

Anisotropy in Quasi-Static Magnetohydrodynamic Turbulence

Mahendra K. Verma

Department of Physics, Indian Institute of Technology Kanpur, Kanpur 208016, India

August 2016

Abstract. In this review we summarise the current status of the quasi-static magnetohydrodynamic turbulence. The energy spectrum is steeper than Kolmogorov's $k^{-5/3}$ spectrum due to the decrease of the kinetic energy flux with wavenumber k as a result of Joule dissipation. The spectral index decreases with the increase of interaction parameter. The flow is quasi two-dimensional with strong \mathbf{U}_\perp at small k and weak U_\parallel at large k , where \mathbf{U}_\perp and U_\parallel are the perpendicular and parallel components of velocity relative to the external magnetic field. For small k , the energy flux of \mathbf{U}_\perp is negative, but for large k , the energy flux of U_\parallel is positive. Pressure mediates the energy transfer from \mathbf{U}_\perp to U_\parallel .

1. Introduction

Magnetohydrodynamics (MHD) deals with the interactions between the flow of electrically conducting fluids and the associated magnetic fields [4, 46]. MHD flows involving plasma are observed in the Sun, stars, solar flares, Tokamak, etc., while those involving liquid metals are found in the core of the Earth; metallurgical applications like surface and stirring controls, instability suppression, liquid metal jets; in the heat exchanger of the proposed International Thermonuclear Experimental Reactor (ITER); and laboratory experiments. The liquid metal flows in territorial experiments typically have low magnetic Reynolds number, and they are often described by quasi-static (QS) MHD. In this review we present the current status of QS MHD turbulence.

In QS MHD, the imposed external magnetic field makes the flow anisotropic. Also, the flow is strongly damped by the Joule dissipation that affects the system properties including the energy spectrum. In addition, the conducting or insulating walls surrounding the fluid have a strong influence on the flow. These effects have been discussed in excellent books [13, 44, 46, 47] and review articles [28, 78]. However, recent works in the field yield interesting insights into the dynamics and anisotropy of QS MHD turbulence. In this review article we cover these new developments. To keep the review focussed, we limit our attention on the bulk flow, and ignore the complexities arising due to walls.

For small and moderate interaction parameters (N), the QS MHD turbulence exhibits power-law energy spectrum ($E(k) \sim k^{-a}$), with the exponent $-a$ decreasing with N . Earlier researchers [22, 25, 29] had attributed the aforementioned steepening of the spectrum (compared to Kolmogorov's spectrum) to the two-dimensionalization of the flow, and related to it to the k^{-3} spectrum of the two-dimensional hydrodynamic turbulence [34]. Several other models have been constructed to explain the steepening of the spectrum. Recently, Verma and Reddy [74] argued that the above phenomena arises because of the decrease of the energy flux with k due to the Joule dissipation; they also showed that the the energy spectrum is exponential ($E(k) \sim \exp(-bk)$) for very large N .

Researchers have shown that the QS MHD flow is quasi two-dimensional with strong perpendicular component of velocity at large length scales and relatively weaker parallel component of velocity at small length scales [1, 8, 18, 19, 58, 77]. The anisotropy of the flow has been quantified using innovative measures such as energy spectrum of the perpendicular and parallel components of the velocity field [76], ring spectrum [10, 19, 58], etc. The energy transfers such as energy flux and ring-to-ring energy transfer too provide valuable insights into the quasi two-dimensional nature of QS MHD turbulence. In this review we focus on the recent developments in the field, in particular the anisotropy of the QS MHD turbulence.

The outline of the paper is as follows: In Section 2 we describe the governing equations of QS MHD in real and Fourier spaces. Section 3 contains discussion on the past and current models of QS MHD, while Sections 4 and 5 describe the primary

experimental and numerical results, respectively. In Section 6 we describe the measures of anisotropy in Fourier space using ring spectrum, while Section 7 contains descriptions of energy flux, shell-to-shell energy transfers, and ring-to-ring transfers. In section 8, we present a model of QS MHD turbulence based on variable energy-flux, as well as review the older models in the light of new findings. Section 9 contains a brief discussion on QS MHD flows in channels and boxes. We conclude in section 10.

2. Governing equations

2.1. MHD equations

The equations of incompressible MHD are [4, 59, 71]

$$\frac{\partial \mathbf{u}}{\partial t} + (\mathbf{u} \cdot \nabla) \mathbf{u} = -\nabla(p/\rho) + \frac{1}{\rho}(\mathbf{J} \times \mathbf{B}) + \nu \nabla^2 \mathbf{u} + \mathbf{f}, \quad (1)$$

$$\frac{\partial \mathbf{B}}{\partial t} + (\mathbf{u} \cdot \nabla) \mathbf{B} = (\mathbf{B} \cdot \nabla) \mathbf{u} + \eta \nabla^2 \mathbf{B}, \quad (2)$$

$$\nabla \cdot \mathbf{u} = 0, \quad (3)$$

$$\nabla \cdot \mathbf{B} = 0, \quad (4)$$

where \mathbf{u} is the velocity field, \mathbf{B} is the magnetic field, \mathbf{J} is the current density, \mathbf{f} is the external forcing, p is the pressure of the fluid, and ν , η , and μ are respectively the kinematic viscosity, magnetic diffusivity, and magnetic permeability of the fluid. We assume the density of the fluid, ρ , to be a constant. Note that $\eta = 1/(\mu\sigma)$, where σ is the electrical conductivity of the fluid. In this review, we employ the SI system of units.

Under the MHD approximation,

$$\mathbf{J} = \frac{1}{\mu} \nabla \times \mathbf{B}. \quad (5)$$

Hence

$$\mathbf{J} \times \mathbf{B} = -\nabla \frac{B^2}{2\mu} + \frac{1}{\mu} (\mathbf{B} \cdot \nabla) \mathbf{B}, \quad (6)$$

substitution of which in Eq. (1) yields

$$\frac{\partial \mathbf{u}}{\partial t} + (\mathbf{u} \cdot \nabla) \mathbf{u} = -\nabla(p_{\text{tot}}/\rho) + \frac{1}{\mu\rho} (\mathbf{B} \cdot \nabla) \mathbf{B} + \nu \nabla^2 \mathbf{u} + \mathbf{f}, \quad (7)$$

where $p_{\text{tot}} = p + B^2/(2\mu)$ is the total pressure. In the later discussion, we will drop the subscript tot from p for brevity. In addition, in the co-moving frame of a fluid element, $\mathbf{J} = \sigma \mathbf{E}^*$, where \mathbf{E}^* is the electric field in the co-moving frame. Using the Lorentz transformation under nonrelativistic limit, $\mathbf{E}^* = \mathbf{E} + \mathbf{u} \times \mathbf{B}$, we obtain

$$\mathbf{J} = \sigma(\mathbf{E} + \mathbf{u} \times \mathbf{B}). \quad (8)$$

Note that \mathbf{E} in the above discussion is the net (sum of internal and external) electric field. Equation (5) yields a constraint on \mathbf{J} :

$$\nabla \cdot \mathbf{J} = 0 \quad (9)$$

that helps us determine \mathbf{E} given \mathbf{u} and \mathbf{B} using Eq. (8).

In the momentum equation [Eq. (7)], $(\mathbf{u} \cdot \nabla)\mathbf{u}$ is the inertial term, $(\mathbf{B} \cdot \nabla)\mathbf{B}/(\mu\rho)$ arises due to the Lorenz force, and $\nu\nabla^2\mathbf{u}$ is the viscous dissipation term. In the induction equation [Eq. (2)], $(\mathbf{u} \cdot \nabla)\mathbf{B}$ and $(\mathbf{B} \cdot \nabla)\mathbf{u}$ terms represent the advection and stretching of magnetic field respectively, and $\eta\nabla^2\mathbf{B}$ is the magnetic diffusion term. The ratio of the nonlinear term, $(\mathbf{u} \cdot \nabla)\mathbf{u}$, and the viscous term, $\nu\nabla^2\mathbf{u}$, is the Reynolds number

$$\text{Re} = \frac{U_0 L_0}{\nu}, \quad (10)$$

where U_0 and L_0 are the characteristic velocity and length scales respectively. The ratio of the nonlinear term of the induction equation [either of $(\mathbf{u} \cdot \nabla)\mathbf{B}$ and $(\mathbf{B} \cdot \nabla)\mathbf{u}$] and the magnetic diffusion term, $\eta\nabla^2\mathbf{B}$, is the magnetic Reynolds number

$$\text{Rm} = \frac{U_0 L_0}{\eta}. \quad (11)$$

The magnetic Prandtl number Pm, defined as

$$\text{Pm} = \frac{\nu}{\eta}, \quad (12)$$

is one of the most important parameters of MHD. Note that $\text{Rm} = \text{RePm}$. In Table 1 we list these parameters for some of the important systems (for detailed discussion, refer to Braginskii [7]). Ionised plasmas are hot, and their transport properties depend on the Coulomb interactions among the ions and electrons. Hence the Prandtl number of plasmas depend critically on temperature, and it could take wide range of values. The kinematic viscosity of liquid metals is quite close to that of water, i.e., $\nu \approx v\lambda \approx 10^{-6} \text{ m}^2/\text{s}$, where v is the speed of the molecules (sound speed $\sim 10^3 \text{ m/s}$) and λ is the mean free path length ($\sim 10^{-9} \text{ m}$). The above formula, strictly valid for a dilute gas, provides a reasonable estimate for ν of water. The electrical conductivity, σ , according to Drude's formula is $ne^2\tau/m_e \approx 10^8 \text{ S/m}$, where n is the number density of electrons in the fluid, e, m_e are respectively the electric charge and mass of the electron, and τ is the mean collision time. Therefore, the magnetic diffusivity of liquid metals is

$$\eta = \frac{1}{\mu\sigma} \approx 10^{-2} \text{ m}^2/\text{s}. \quad (13)$$

Hence the Prandtl number of a liquid metal can be estimated as $\nu/\eta \approx 10^{-4}$. We can also estimate the above Prandtl number using

$$\begin{aligned} \text{Pm} &= \frac{\nu}{\eta} \approx v\lambda\mu\sigma \\ &\approx \frac{\mu_0\epsilon_0 e^2}{\epsilon_0 m_e \lambda} n\lambda^3 \approx \frac{e^2}{c^2 \epsilon_0 m_e \lambda} \\ &\approx \frac{e^2}{\hbar c \epsilon_0} \frac{\hbar}{m_e c} \frac{1}{\lambda} \approx \frac{4\pi}{137} \frac{L_{\text{Compton}}}{\lambda} \approx 10^{-4}. \end{aligned} \quad (14)$$

Here we use $v\tau = \lambda$, $\hbar = h/2\pi$ is the reduced Planck constant, $e^2/(4\pi\epsilon_0\hbar c)$ is the fine structure constant, $L_{\text{Compton}} \approx 10^{-12} \text{ m}$ is the Compton wavelength, and $\lambda \sim 10^{-9} \text{ m}$ is the mean free-path length. In particular, the respective Prandtl numbers of liquid

Sodium, Gallium, Galinstan, Mercury, Molten Iron are approximately 0.88×10^{-5} , 1.5×10^{-6} , 1.4×10^{-6} , 1.4×10^{-7} , 10^{-6} .

The flow behaviour depends quite crucially on the system parameters. We classify them in four regimes:

- (i) $Re \ll 1$ and $Rm \ll 1$: Dissipative MHD.
- (ii) $Re \gg 1$ and $Rm \ll 1$: Liquid-metal low- Rm MHD flows for which $Pm = Rm/Re \ll 1$. Typical laboratory systems come under this category. The quasi-static MHD is a limiting case of such flows when $Rm = 0$. In this review, we will focus on this regime.
- (iii) $Re \ll 1$ and $Rm \gg 1$: Laminar plasma flows for which $Pm \gg 1$. Such flows are observed in laminar dynamos [43].
- (iv) $Re \gg 1$ and $Rm \gg 1$: Turbulent MHD, examples of which are the Earth's outer core, solar wind, solar convection zone, sunspots, and interstellar medium [71, 43] (refer to Table 1 for the parameters). Note that such systems could exhibit self-induced magnetic field (dynamo) since the magnetic Reynolds number is greater than unity for them [43, 45].

Table 1. For some important systems, the Prandtl number Pm , the Reynolds number Re , and magnetic Reynolds number Rm .

System	Pm	Re	Rm
liquid metal experiments (terrestrial)	10^{-7} – 10^{-6}	10^3 – 10^4	10^{-4} – 10^{-2}
Earth's outer core	10^{-6}	10^9	10^3
Sunspots	10^{-3}	10^{12}	10^9
Interstellar media	10^{12}	10^3	10^{15}

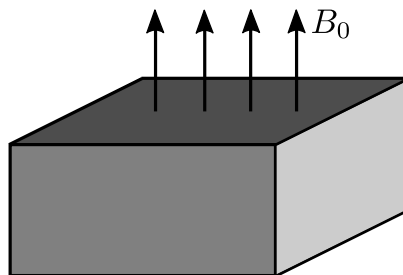


Figure 1. A schematic diagram exhibiting a magnetofluid under the influence of a constant external magnetic field $B_0 \hat{z}$. The velocity field at the walls could satisfy periodic or no-slip boundary condition.

On many occasions, plasmas or liquid metals are subjected to a constant external magnetic field (denoted by \mathbf{B}_0). In the schematic diagram shown in Fig. 1, \mathbf{B}_0 points

along \hat{z} . For such systems, the magnetic field of Eqs. (7, 2) can be decomposed into its mean, \mathbf{B}_0 , and fluctuation, \mathbf{b} , i.e., $\mathbf{B} = \mathbf{B}_0 + \mathbf{b}$. We rewrite Equations (2–4,7) in terms of \mathbf{B}_0 and \mathbf{b} as

$$\begin{aligned} \frac{\partial \mathbf{u}}{\partial t} + (\mathbf{u} \cdot \nabla) \mathbf{u} = & -\nabla(p/\rho) + \frac{1}{\mu\rho}(\mathbf{B}_0 \cdot \nabla) \mathbf{b} + \frac{1}{\mu\rho}(\mathbf{b} \cdot \nabla) \mathbf{b} \\ & + \nu \nabla^2 \mathbf{u} + \mathbf{f}, \end{aligned} \quad (15)$$

$$\frac{\partial \mathbf{b}}{\partial t} + (\mathbf{u} \cdot \nabla) \mathbf{b} = (\mathbf{b} \cdot \nabla) \mathbf{u} + (\mathbf{B}_0 \cdot \nabla) \mathbf{u} + \eta \nabla^2 \mathbf{b}, \quad (16)$$

$$\nabla \cdot \mathbf{u} = 0, \quad (17)$$

$$\nabla \cdot \mathbf{b} = 0. \quad (18)$$

Shebalin [62] and Teaca *et al* [68] analyzed the induced anisotropy by the mean magnetic field \mathbf{B}_0 . One of the features of such flows is that the velocity along \mathbf{B}_0 is suppressed. This is a common feature of anisotropic MHD turbulence and anisotropic QS MHD turbulence.

The aforementioned equations get simplified further in the presence of a strong external magnetic field, and when $\text{Rm} \rightarrow 0$. This system is the *quasi-static MHD*, a topic of this review. We will quantify B_0 -induced anisotropy in such flows.

In the next subsection we will describe the governing equations of QS MHD.

2.2. QS MHD

The magnetic Reynolds number $\text{Rm} = U_0 L_0 / \eta$. Hence, $\text{Rm} \rightarrow 0$ when $\eta \rightarrow \infty$ (or $\text{Pm} \rightarrow 0$), and U_0 and L_0 take moderate values (in contrast, large U_0 and L_0 in planetary or astrophysical systems yield large Rm). However, the Reynolds number $\text{Re} = \text{Rm}/\text{Pm}$ is nonzero. Liquid metal flows with large Re are turbulent.

The magnetic Reynolds number is the ratio of the nonlinear term of the induction equation and the magnetic diffusion. Hence in the limit $\text{Rm} \rightarrow 0$, the nonlinear terms of the induction equation [Eq. (16)] can be ignored compared to the diffusion term, thus Eq. (16) reduces to

$$\frac{\partial \mathbf{b}}{\partial t} = (\mathbf{B}_0 \cdot \nabla) \mathbf{u} + \eta \nabla^2 \mathbf{b}. \quad (19)$$

The Fourier representation of Eq. (19) is

$$\frac{\partial \hat{\mathbf{b}}(\mathbf{k})}{\partial t} + \eta k^2 \hat{\mathbf{b}}(\mathbf{k}) = [(\widehat{\mathbf{B}_0 \cdot \nabla}) \mathbf{u}](\mathbf{k}) = \hat{\mathbf{f}}(\mathbf{k}, t) \quad (20)$$

where $\hat{\cdot}$ represents the Fourier transform. The solution of the above equation is

$$\hat{\mathbf{b}}(\mathbf{k}, t) = \left(\hat{\mathbf{b}}(\mathbf{k}, 0) - \frac{\hat{\mathbf{f}}(\mathbf{k}, t)}{\eta k^2} \right) \exp(-\eta k^2 t) + \frac{\hat{\mathbf{f}}(\mathbf{k}, t)}{\eta k^2}, \quad (21)$$

where $\hat{\mathbf{b}}(\mathbf{k}, 0)$ is the initial magnetic field. For large η , $\exp(-\eta k^2 t) \rightarrow 0$, and hence

$$\hat{\mathbf{b}}(\mathbf{k}, t) = \frac{\hat{\mathbf{f}}(\mathbf{k}, t)}{\eta k^2} = \frac{[(\widehat{\mathbf{B}_0 \cdot \nabla}) \mathbf{u}](\mathbf{k})}{\eta k^2}, \quad (22)$$

which is the solution of Eq. (20) with $\partial \hat{\mathbf{b}}(\mathbf{k})/\partial t = 0$. This is the *quasi-static approximation* [28, 46]. Physically, the large magnetic diffusivity quickly suppresses the transients [the first term of Eq. (21)], and hence the induced magnetic field is proportional to $\mathbf{f}(\mathbf{k})$. In real space, the resulting induction equation can be written as

$$\eta \nabla^2 \mathbf{b} = -(\mathbf{B}_0 \cdot \nabla) \mathbf{u}, \quad (23)$$

which is Poisson's equation that yields a unique solution for \mathbf{b} given the source term, $-(\mathbf{B}_0 \cdot \nabla) \mathbf{u}$, and the boundary condition. We write the solution (\mathbf{b}) symbolically as

$$\mathbf{b} = -\Delta^{-1} \left[\frac{1}{\eta} (\mathbf{B}_0 \cdot \nabla) \mathbf{u} \right], \quad (24)$$

where Δ^{-1} is the inverse of the Laplacian operator. Here η is considered to be a constant in space.

Thus, under QS approximation, for the lowest wavenumber ($k \sim 1/L$) or large length scales,

$$\frac{b}{B_0} \approx \frac{UL}{\eta} = \text{Rm} \ll 1. \quad (25)$$

Since $b \ll B_0$, in Eq. (15), we ignore the $(\mathbf{b} \cdot \nabla) \mathbf{b}/(\mu\rho)$ term compared to the $(\mathbf{B}_0 \cdot \nabla) \mathbf{b}/(\mu\rho)$. Hence Eq. (15) becomes

$$\frac{\partial \mathbf{u}}{\partial t} + (\mathbf{u} \cdot \nabla) \mathbf{u} = -\nabla(p/\rho) + \frac{1}{\mu\rho} (\mathbf{B}_0 \cdot \nabla) \mathbf{b} + \nu \nabla^2 \mathbf{u} + \mathbf{f}. \quad (26)$$

Substitution of Eq. (24) in Eq. (26) yields the QS MHD equations:

$$\frac{\partial \mathbf{u}}{\partial t} + (\mathbf{u} \cdot \nabla) \mathbf{u} = -\nabla(p/\rho) - \frac{\sigma}{\rho} \Delta^{-1} [(\mathbf{B}_0 \cdot \nabla)^2 \mathbf{u}] + \nu \nabla^2 \mathbf{u} + \mathbf{f}, \quad (27)$$

$$\nabla \cdot \mathbf{u} = 0. \quad (28)$$

If \mathbf{B}_0 is along the z -direction, then the Lorentz force term of Eq. (27) can be written as [28, 46]

$$-\frac{\sigma}{\rho} \Delta^{-1} [(\mathbf{B}_0 \cdot \nabla)^2 \mathbf{u}] = -\frac{\sigma B_0^2}{\rho} \Delta^{-1} \left[\frac{\partial^2 \mathbf{u}}{\partial z^2} \right]. \quad (29)$$

We solve Eq. (27,28) given boundary condition and initial condition.

Under the quasi-static limit,

$$\nabla \times \mathbf{E} = -\frac{\partial \mathbf{b}}{\partial t} \approx 0, \quad (30)$$

hence we can write $\mathbf{E} = -\nabla\phi$, where ϕ is the electric potential. Substitution of $\mathbf{E} = -\nabla\phi$ in Eq. (8) yields the current density

$$\mathbf{J} = \sigma(-\nabla\phi + \mathbf{u} \times \mathbf{B}_0). \quad (31)$$

Using the constraint $\nabla \cdot \mathbf{J} = 0$ we obtain

$$\nabla^2 \phi = \nabla \cdot (\mathbf{u} \times \mathbf{B}_0), \quad (32)$$

which is Poisson's equation. We solve the above equation for a given boundary condition that yields ϕ , substitution of which in Eq. (31) yields \mathbf{J} . Once \mathbf{J} has been determined, we can solve for the velocity field using the following equation:

$$\frac{\partial \mathbf{u}}{\partial t} + (\mathbf{u} \cdot \nabla) \mathbf{u} = -\nabla(p/\rho) + \frac{1}{\rho}(\mathbf{J} \times \mathbf{B}_0) + \nu \nabla^2 \mathbf{u} + \mathbf{f} \quad (33)$$

This general strategy is followed for solving bounded QS MHD flows.

Note that Eq. (24) yields \mathbf{b} in terms of \mathbf{u} ; this \mathbf{b} is substituted in Eq. (26), whose solution yields $\mathbf{u}(t)$. The second approach, which is based on scalar potential ϕ , is slightly different. Here, \mathbf{J} , computed using Eq. (31), is substituted for the Lorentz force term $\mathbf{J} \times \mathbf{B}_0$ of Eq. (33). The boundary conditions for wall-bounded flows are handled somewhat differently in these two approaches. The formulation based on \mathbf{b} allows some freedom in the choice of boundary condition for wall-bounded flows. This issue and the uniqueness of the induced currents are discussed in a recent paper by Bandaru *et al* [2].

For QS MHD, we define another important nondimensional number called the *interaction parameter*, N , which is the ratio of the Lorentz force $(\sigma/\rho)\Delta^{-1}[(\mathbf{B}_0 \cdot \nabla)^2 \mathbf{u}]$ and the nonlinear term $(\mathbf{u} \cdot \nabla) \mathbf{u}$, i.e.,

$$N = \frac{\sigma B_0^2 L_0}{\rho u_{\text{rms}}}. \quad (34)$$

This parameter plays an important role in determining the flow properties. The diffusion time of the kinetic energy due to the Lorentz force is $t_J = \rho/(\sigma B_0^2)$, and the eddy turnover time is $t_{\text{eddy}} = L_0/u_{\text{rms}}$. Hence the interaction parameter can also be written as

$$N = \frac{t_{\text{eddy}}}{t_J}. \quad (35)$$

We nondimensionalize the above equations using the characteristic velocity U_0 as the velocity scale, the size of the box L_0 as the length scale, and L_0/U_0 as the time scale, which yields

$$\frac{\partial \mathbf{U}}{\partial t'} + (\mathbf{U} \cdot \nabla') \mathbf{U} = -\nabla' P - B_0'^2 \Delta'^{-1} \left[\frac{\partial^2 \mathbf{U}}{\partial Z'^2} \right] + \nu' \nabla'^2 \mathbf{U} + \mathbf{F}, \quad (36)$$

$$\nabla' \cdot \mathbf{U} = 0, \quad (37)$$

where the nondimensionalized variables are $\mathbf{U} = \mathbf{u}/U_0$, $\nabla' = L_0 \nabla$, $t' = t(U_0/L_0)$, $B_0'^2 = \sigma B_0^2 L_0/(\rho U_0)$, $\mathbf{F} = \mathbf{f}L/U_0^2$, $P = p/(\rho U_0^2)$, and $\nu' = \nu/(U_0 L_0)$. In terms of the nondimensional variables, the interaction parameter is

$$N = \frac{B_0'^2 L'}{U'} \quad (38)$$

where U' is the rms value of \mathbf{U}' , and L' is the correlation or integral length of the flow in the nondimensional box; both U' and L' will be defined subsequently. It is important to note that $B_0'^2$ is not same as N , but they are of the same order since U' and L' are of the order unity. We remark that in the subsequent discussion we drop the prime from t' .

In this review, we treat B'_0 as an input parameter, while N as the response parameter. The difference becomes significant particularly for decaying turbulence where N can change significantly with time. Some authors characterise the interaction parameter using the initial values of rms velocity and integral length scale (see, e.g., [19, 79]). Note however that for decaying turbulence, the instantaneous N will differ from the initial N . In this review we report the values of N at the steady-state, rather than N at $t = 0$ [58]. We denote initial interaction parameter using a separate parameter N_0 . We also remark that the Reynolds number in terms of nondimensional variable is

$$Re = \frac{U'L'}{\nu'}. \quad (39)$$

2.3. QS MHD equations in the Fourier space

Fourier space representation is often employed in turbulence research since it captures the scale-by-scale interactions of the flow. It is also useful to quantify the energy contents at various scales. Transformation of Eqs. (36) and (37) to Fourier space yields [27, 28, 46, 61, 79]:

$$\begin{aligned} \frac{\partial \hat{U}_i(\mathbf{k})}{\partial t'} &= -ik_j \sum_{\mathbf{q}} \hat{U}_j(\mathbf{q}) \hat{U}_i(\mathbf{k} - \mathbf{q}) - ik_i \hat{P}(\mathbf{k}) - B_0'^2 \cos^2(\theta) \hat{U}_i(\mathbf{k}) \\ &\quad - \nu' k^2 \hat{U}_i(\mathbf{k}) + \hat{F}_i(\mathbf{k}), \end{aligned} \quad (40)$$

$$k_i \hat{U}_i(\mathbf{k}) = 0, \quad (41)$$

where $\hat{U}_i(\mathbf{k})$, $\hat{F}_i(\mathbf{k})$ are the Fourier transforms of the i^{th} components of the velocity and force fields respectively, $\hat{P}(\mathbf{k})$ is the Fourier transform of the pressure field, and θ is the angle between the wavenumber vector \mathbf{k} and the external magnetic field \mathbf{B}_0 . Refer to Fig. 2(a) for an illustration. The convolution term, $-ik_j \sum \hat{U}_j(\mathbf{q}) \hat{U}_i(\mathbf{k} - \mathbf{q})$, arises due to the nonlinear interactions, and it is responsible for the energy transfers from one scale to another. Here we assume Einstein convention for the indices according to which the repeated indices are summed. [Also, for brevity we drop the prime of \$t'\$ in subsequent discussion.](#)

It is convenient and insightful to decompose the velocity field using the basis function $(\hat{e}_1, \hat{e}_2, \hat{e}_3)$ shown in Fig. 2(b):

$$\hat{e}_3 = \hat{k}; \quad \hat{e}_1 = \hat{k} \times \hat{z}; \quad \hat{e}_2 = \hat{e}_3 \times \hat{e}_1; \quad (42)$$

where \hat{k} is the unit vector along \mathbf{k} , and \hat{z} is the unit vector along \mathbf{B}_0 . Due the incompressibility condition, $\mathbf{k} \cdot \hat{\mathbf{U}}(\mathbf{k}) = 0$, the velocity component along \hat{e}_3 vanishes, and

$$\hat{\mathbf{U}}(\mathbf{k}) = \hat{U}^{(1)}(\mathbf{k}) \hat{e}_1 + \hat{U}^{(2)}(\mathbf{k}) \hat{e}_2. \quad (43)$$

The components $\hat{U}^{(1)}$ and $\hat{U}^{(2)}$ are called *toroidal* and *poloidal* modes of the field.

The energy of a Fourier mode \mathbf{k} , also called *modal energy*, is

$$E(\mathbf{k}) = \frac{1}{2} |\hat{\mathbf{U}}(\mathbf{k})|^2, \quad (44)$$

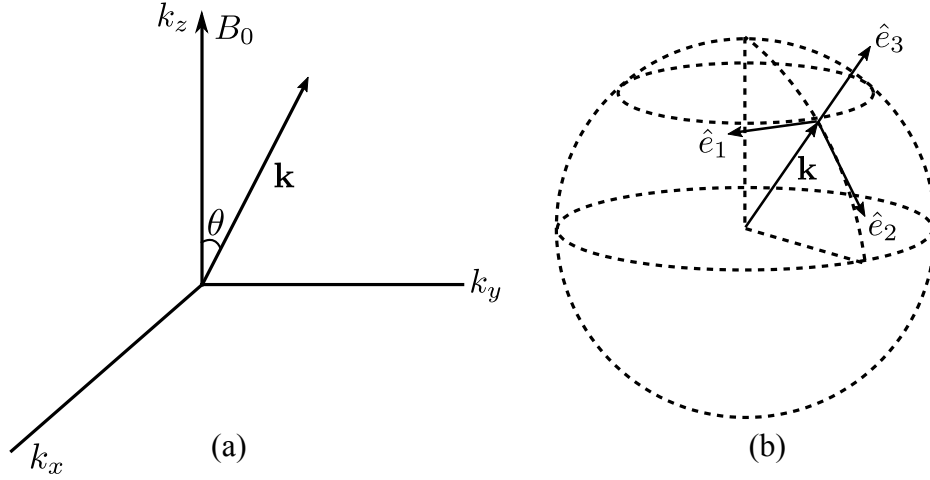


Figure 2. (a) A wavenumber \mathbf{k} in Fourier space. The velocity field $\hat{\mathbf{U}}(\mathbf{k})$ is perpendicular to \mathbf{k} . (b) Toroidal and poloidal decomposition of a Fourier mode. The external magnetic field is along the z axis.

and its evolution in Fourier space is

$$\frac{\partial E(\mathbf{k})}{\partial t} = T(\mathbf{k}) - 2B_0'^2 \cos^2(\theta) E(\mathbf{k}) - 2\nu' k^2 E(\mathbf{k}) + \mathcal{F}(\mathbf{k}), \quad (45)$$

where $T(\mathbf{k})$ is the rate of the nonlinear energy transfer to the mode \mathbf{k} , and $\mathcal{F}(\mathbf{k})$ is the energy supply rate by the external forcing \mathbf{F} :

$$T(\mathbf{k}) = \Re\left\{-ik_j \sum \hat{U}_j(\mathbf{q}) \hat{U}_i(\mathbf{k} - \mathbf{q})\right\} \hat{U}_i^*(\mathbf{k}) \quad (46)$$

$$\mathcal{F}(\mathbf{k}) = \Re\left[\hat{F}_i(\mathbf{k}) \hat{U}_i^*(\mathbf{k})\right], \quad (47)$$

where \Re stands for the real part of the argument. Note that the pressure does not appear in the energy equation due to the incompressibility condition $\mathbf{k} \cdot \hat{\mathbf{U}}(\mathbf{k}) = 0$ [71].

The other two terms of Eq. (45) are the dissipative terms—the Joule dissipation rate

$$\epsilon_J(\mathbf{k}) = 2B_0'^2 \cos^2(\theta) E(\mathbf{k}), \quad (48)$$

and the viscous dissipation rate

$$\epsilon_\nu(\mathbf{k}) = 2\nu' k^2 E(\mathbf{k}). \quad (49)$$

Note that ϵ_J is the energy transferred from the velocity field to the magnetic field, which is instantaneously dissipated due to large magnetic diffusivity η . Also, the Joule dissipation is active at all scales, unlike the viscous dissipation rate that dominates at small scales.

We also define one-dimensional energy spectrum $E(k)$ using [38]

$$E = \int_0^\infty E(k) dk = \int E(\mathbf{k}) d\mathbf{k} = \frac{3}{2} U^2. \quad (50)$$

The above equation also implies that

$$E(k) = \sum_{k-1 < k' \leq k} E(\mathbf{k}). \quad (51)$$

The integral length scale of the system, which is a measure of the velocity correlation length, is defined as [10, 77]

$$L = \frac{\pi}{(2U^2)} \int_0^\infty (E(k)/k) dk. \quad (52)$$

The eddy-turnover time is defined as $\tau = L/U$.

In a three-dimensional hydrodynamic turbulence, the term $T(k)$ facilitates energy transfer from small wavenumber modes to large wavenumber modes. A collective effect of this transfer is a net energy flux from a wavenumber sphere, which is defined as [33, 38]

$$\Pi(k) = - \int_0^k T(k') dk' \quad (53)$$

or

$$T(k) = - \frac{d\Pi(k)}{dk}. \quad (54)$$

We assume that the flow is in a steady state ($dE(\mathbf{k})/dt = 0$). Substitution of Eq. (54) in Eq. (45) and a summation over the modes in a shell of radius k yield

$$\frac{d\Pi(k)}{dk} = -\epsilon_\nu(k) - \epsilon_J(k) + F(k). \quad (55)$$

Note that the external force $\mathbf{F}(k)$ is expected to be active only at small wavenumbers or large scales. Thus, for $k > k_f$, where k_f is the forcing wavenumber, $F(k) = 0$. In this regime, the flux $\Pi(k)$ will decrease with k since $\epsilon_J(k)$ is active at all scales [57, 58, 72, 74]. This result is contrary to the constant energy flux observed in fluid turbulence in which ϵ_ν is effective only at large k 's (also see Sec. 2.5). The aforementioned decrease of $\Pi(k)$ has major impact on the energy spectrum of QS MHD, as well as on the anisotropy of the flow (to be discussed in Sections 5 and 8 respectively). This kind of steepening of the energy flux and spectrum are also observed in hydrodynamic turbulence with Ekman friction. Verma [72] showed that in the presence of Ekman friction, the enstrophy flux of two-dimensional hydrodynamic turbulence decreases with k , while the energy spectrum $E(k)$ is steeper than k^{-3} corresponding to that of 2D hydrodynamic turbulence in the constant enstrophy-flux regime.

In this review we focus on the description of anisotropy in QS MHD arising due to the external magnetic field. We will quantify anisotropy using the energy spectrum and energy transfer diagnostics. Our work will be focussed on a Fourier space description since it captures scale-by-scale anisotropy; this quantity is inaccessible in a real space representation. In the Fourier space, we study the angular-dependent ring spectrum and ring-to-ring to energy transfers., in addition to standard diagnostics like energy spectrum and flux.

It is important to state the energy equation in dimensional form since many analytical works use this equation:

$$\frac{\partial E(\mathbf{k})}{\partial t} = T(\mathbf{k}) - \frac{2\sigma B_0^2}{\rho} \cos^2(\theta) E(\mathbf{k}) - 2\nu k^2 E(\mathbf{k}) + F(\mathbf{k}). \quad (56)$$

Also, in Fourier space Eq. (24) translates to

$$\hat{\mathbf{b}}(\mathbf{k}) = \frac{i(\mathbf{B}_0 \cdot \mathbf{k})}{\eta k^2} \hat{\mathbf{u}}(\mathbf{k}). \quad (57)$$

After a detailed discussion on the formalism of QS MHD, we provide a qualitative description of its dynamics.

2.4. Dynamics in QS MHD: a qualitative picture

The Lorentz force on a fluid element in QS MHD is

$$\mathbf{f}_L = \mathbf{J} \times \mathbf{B} \approx \sigma(\mathbf{E} + \mathbf{u} \times \mathbf{B}_0) \times \mathbf{B}_0. \quad (58)$$

Clearly \mathbf{f}_L is perpendicular to \mathbf{B}_0 . Equation (40) however appears to indicate that \mathbf{f}_L is in the direction of $-\mathbf{u}$, but it is not the case due to the $-\nabla B^2/(2\mu)$ term [see Eq. (6)]. In Fourier space

$$\begin{aligned} \mathbf{f}_L(\mathbf{k}) &= \hat{\mathbf{J}}(\mathbf{k}) \times \mathbf{B}_0 \\ &= i(\mathbf{k} \times \hat{\mathbf{b}}(\mathbf{k})) \times \mathbf{B}_0 \\ &= -\frac{(\mathbf{B}_0 \cdot \mathbf{k})}{\eta k^2} (\mathbf{k} \times \hat{\mathbf{u}}(\mathbf{k})) \times \mathbf{B}_0 \\ &= \frac{(\mathbf{B}_0 \cdot \mathbf{k})}{\eta k^2} [\mathbf{k}(\hat{\mathbf{u}}(\mathbf{k}) \cdot \mathbf{B}_0) - \hat{\mathbf{u}}(\mathbf{k})(\mathbf{k} \cdot \mathbf{B}_0)]. \end{aligned} \quad (59)$$

Clearly $\mathbf{f}_L(\mathbf{k}) \cdot \mathbf{B}_0 = 0$, hence $\mathbf{f}_L(\mathbf{r}) \cdot \mathbf{B}_0 = [\sum_{\mathbf{k}} \mathbf{f}_L(\mathbf{k}) \exp(i\mathbf{k} \cdot \mathbf{r})] \cdot \mathbf{B}_0 = 0$. Thus $\mathbf{f}_L(\mathbf{r})$ (in real space) is perpendicular to \mathbf{B}_0 . For large B_0 or N , \mathbf{f}_L dominates the nonlinear term $\mathbf{u} \cdot \nabla \mathbf{u}$ and the pressure gradient. The Lorentz force being in the xy plane is one of the primary reasons for the quasi two-dimensionalization of QS MHD turbulence.

Equation (59) shows that $\mathbf{f}_L(\mathbf{k}) \propto \mathbf{B}_0 \cdot \mathbf{k}$, hence $\mathbf{f}_L(k_x, k_y, 0) = 0$, i.e., $\mathbf{f}_L(\mathbf{k})$ in the $k_z = 0$ plane vanishes. Thus, in the $k_z = 0$ plane, the nonlinear term $\mathbf{u} \cdot \nabla \mathbf{u}(\mathbf{k})$ dominates the other terms, and the flow behaviour has similarities with those in two-dimensional (2D) hydrodynamic turbulence. We caution however that $u_z \neq 0$ in QS MHD turbulence, thus making the flow quasi two-dimensional. Hence, QS MHD turbulence is more complex than 2D hydrodynamic turbulence. Also note that the Fourier modes $\mathbf{u}(\mathbf{k})$ with $k_z \neq 0$ are suppressed by the Joule dissipation term that increases with N . A combination of the aforementioned effects leads to quasi two-dimensionalization of the QS MHD flow for large N .

The QS MHD turbulence differs significantly from Alfvénic turbulence. For example, Alfvénic turbulence has large Rm or very small η , contrary to QS MHD turbulence for which $\text{Rm} \rightarrow 0$ or $\eta \rightarrow \infty$. The linearized QS MHD equation is

$$\frac{\partial \hat{U}_i(\mathbf{k})}{\partial t} = -B_0'^2 \cos^2(\theta) \hat{U}_i(\mathbf{k}), \quad (60)$$

whose solution yields the following linear mode of QS MHD:

$$\hat{U}_i(\mathbf{k}) = \exp(-B_0'^2 t \cos^2 \theta). \quad (61)$$

This dissipative mode is very different from an Alfvén wave, which is a solution of the linear Alfvénic MHD with $\nu = \eta = 0$ [4, 46]. In QS MHD, the kinetic energy is directly transferred to the Joule dissipation, and it does not support any MHD wave.

In Alfvénic turbulence, $\eta \rightarrow 0$ or $\sigma \rightarrow \infty$. Hence,

$$\mathbf{E} + \mathbf{u} \times \mathbf{B}_0 = \frac{\mathbf{J}}{\sigma} \approx 0. \quad (62)$$

However for QS MHD,

$$\mathbf{E} + \mathbf{u} \times \mathbf{B}_0 = \frac{\mathbf{J}}{\sigma} \neq 0 \quad (63)$$

since σ is finite.

In this review we will discuss energy spectrum and flux of the bulk flow of QS MHD turbulence. The phenomena to be discussed are strongly motivated from the hydrodynamic turbulence. Hence, in the next subsection we introduce the phenomenology of hydrodynamics turbulence briefly.

2.5. A brief introduction to hydrodynamic turbulence phenomenology

Most of the flows in laboratory experiments and terrestrial atmosphere can be considered to be incompressible since the density variation in such flows is only a small fraction of the mean density. Therefore, such hydrodynamic flows are described by Navier-Stokes equation:

$$\frac{\partial \mathbf{u}}{\partial t} + (\mathbf{u} \cdot \nabla) \mathbf{u} = -\nabla(p/\rho) + \nu \nabla^2 \mathbf{u} + \mathbf{f}, \quad (64)$$

$$\nabla \cdot \mathbf{u} = 0. \quad (65)$$

The flow becomes turbulent when the nonlinear term is much larger than the viscous term, or when $\text{Re} = UL/\nu \gg 1$. Without loss of generality, we take $\rho = 1$.

Modelling turbulent flow has been a key problems of physics. One of the most acclaimed theory of turbulence is by Kolmogorov [31]. Here external force \mathbf{f} is assumed to be active at large length scales (of the order of system size), i.e. for $k = k_f \sim 1/L$. The energy supplied by \mathbf{f} cascades to smaller scales, and finally it is dissipated at the dissipation scales. When we employ Eq. (55) to hydrodynamic turbulence for $k > k_f$, we have $\epsilon_J = 0$, and the energy supply rate by the external force $F(k) = 0$. Therefore

$$\frac{d\Pi(k)}{dk} = \epsilon_\nu = -2\nu k^2 E(k). \quad (66)$$

For turbulent flows, the viscous dissipation dominates in the dissipation range, i.e. for $k > k_d$, where k_d is the dissipation wavenumber. Therefore, in the wavenumber band $k_f < k < k_d$, called the *inertial range*, $F(k), D(k) \rightarrow 0$, and hence Eq. (55) yields $d\Pi/dk \approx 0$. Therefore the energy flux remains an approximate constant in the inertial range, i.e.,

$$\Pi(k) = \Pi = \text{const}, \quad (67)$$

and it equals the total dissipation rate.

Now, using dimensional analysis, one can derive the one-dimensional energy spectrum as

$$E(k) = K_{K_o} \Pi^{2/3} k^{-5/3} \quad (68)$$

where K_{K_o} is the Kolmogorov's constant. Numerical simulations, experiments, and analytical tools report that $K_{K_o} \approx 1.6$.

The space dimension does not appear explicitly in the above set of arguments, hence we may expect Eqs. (67,68) to describe both two-dimensional and three-dimensional (3D) flows. Three-dimensional hydrodynamic turbulence exhibits $\Pi(k)$ and $E(k)$ given by Eqs. (67,68) respectively, but these formulae are not valid in 2D hydrodynamic turbulence. In inviscid 2D hydrodynamics (with $\nu = 0$), the total energy, $u^2/2$, and the total enstrophy, $\omega^2/2$, are conserved, contrary to 3D hydrodynamics in which only the total energy is conserved. The aforementioned conservation laws for 2D hydrodynamics leads to very different turbulence phenomenology in 2D [34]. Here the fluid is forced at $k_f \gg 1/L$. Kraichnan [34] showed that in 2D hydrodynamic turbulence, for $k < k_f$,

$$E(k) = K_{2D} \Pi^{2/3} k^{-5/3}, \quad \Pi = \text{const} < 0, \quad (69)$$

where K_{2D} is a constant, and Π is the energy flux. However for $k > k_f$,

$$E(k) = K'_{2D} \Pi_\omega^{2/3} k^{-3}, \quad \Pi_\omega = \text{const} > 0, \quad (70)$$

where Π_ω is the enstrophy flux, and K'_{2D} is another constant. Note that in 2D hydrodynamic turbulence, the kinetic energy exhibits an inverse cascade, while the enstrophy flux shows a forward cascade.

In the paper, we show that for small interaction parameter N ($N \lesssim 1$), QS MHD turbulence has similarities with 3D hydrodynamic turbulence, with the spectral exponent close to $-5/3$. However for large N , the energy spectrum is steeper than $k^{-5/3}$, and the spectral exponent decreases with N , reaching as low as $\approx (-5)$ for intermediate N (e.g. $N = 27$). For very large N , the energy spectrum of QS MHD turbulence becomes exponential, i.e. $E(k) \sim \exp(-bk)$ where b is a constant.

In engineering applications and in planetary interiors, the QS magnetofluid is often confined between walls [46, 47] that have significant effects on the flow, which will be discussed briefly in Sec. 9. The present section does not contain any discussion on the walls. In this review we focus on the bulk flow in QS MHD where the aforementioned equations provide adequate description.

In the next section we will describe some of the analytical models of QS MHD turbulence.

3. Analytical Models of QS MHD turbulence

The equations of QS MHD are nonlinear, hence their general analytical solution is not available. In the past, researchers have constructed models for QS MHD turbulence some of which will be described below. Keeping in mind the theme of the review, we will focus on the models for the bulk flow.

Moffatt [42] and Schumann [61] were one of the first to model the energy distribution in QS MHD. They imagined an isotropic magnetofluid in which an external magnetic field is suddenly turned on. They studied how the fluid energy in such flows decays with time. In the early stages, the velocity correlation function is described by an isotropic second-rank tensor:

$$\langle \hat{u}_i(\mathbf{k}, t) \hat{u}_j^*(\mathbf{k}, t) \rangle = \phi_{ij}(\mathbf{k}, t) = \left(\delta_{ij} - \frac{k_i k_j}{k^2} \right) E(\mathbf{k}), \quad (71)$$

where $E(\mathbf{k})$ is as defined in Equation (44), and δ_{ij} is the Kronecker delta function. Moffatt [42] assumed that for sufficiently large N and small ν (large Reynolds number), the nonlinear energy transfer $T(k)$ is weak compared to the Lorentz force. Hence he modelled the energy equation for the decaying QS MHD turbulence as [see Eq. (56)]

$$\frac{\partial E(\mathbf{k})}{\partial t} = -\frac{2\sigma B_0^2}{\rho} E(\mathbf{k}) \cos^2 \theta. \quad (72)$$

Note that θ is a function of \mathbf{k} . According to the above, the energy is dissipated more strongly near the polar region ($\theta \approx 0$) than the equatorial region. The solution of the above equation is

$$E(\mathbf{k}, t) = E(\mathbf{k}, 0) \exp\left(-2\cos^2 \theta \frac{t}{t_J}\right), \quad (73)$$

where $t_J = \rho/(\sigma B_0^2)$ is the kinetic-energy diffusion time-scale due to the Lorentz force.

At time t , the spectrum is effectively damped for $\theta < \theta_c$ where

$$\cos \theta_c = \sqrt{t_J/t}. \quad (74)$$

Moffatt [42] derived the evolution of the total energy as

$$\begin{aligned} E(t) &= \int E(\mathbf{k}, 0) \exp\left(-2\cos^2 \theta \frac{t}{t_J}\right) d\mathbf{k} \\ &= \int k^2 dk d(\cos \theta) d\phi E(\mathbf{k}, 0) \exp\left(-2\cos^2 \theta \frac{t}{t_J}\right) \\ &= \sqrt{\frac{t_J}{t}} \int k^2 dk d\left(\cos \theta \sqrt{\frac{t}{t_J}}\right) d\phi E(\mathbf{k}, 0) \exp\left(-2\cos^2 \theta \frac{t}{t_J}\right) \\ &= K \sqrt{\frac{t_J}{t}}, \end{aligned} \quad (75)$$

where K is value of the integral of the third line, whose dimension is u^2 . In the last step of the above equation, we make a change of variable from $\cos \theta$ to $\cos \theta \sqrt{t/t_J}$. Thus, Moffatt [42] argued that the total energy of QS MHD decays as $t^{-1/2}$. Since Moffatt [42] and Schumann [61] ignored the nonlinear term in the above derivation, the above decay law is said to be applicable in the *linear regime*. The above assumption is clearly invalid at $\theta \approx \pi/2$, where the nonlinear term $\mathbf{u} \cdot \nabla \mathbf{u}$ is the most dominant term. We will discuss these issues in Sec. 8.

Using Eq. (71), Moffatt [42] concluded that

$$E_{\parallel} = \frac{1}{2}u_z^2 = \frac{1}{2} \left(1 - \frac{k_z^2}{k^2}\right) E(k) = \frac{1}{2}(1 - \cos^2 \theta)E(k), \quad (76)$$

$$E_{\perp} = \frac{1}{2}(u_x^2 + u_y^2) = \frac{1}{2} \left[2 - \frac{k_x^2 + k_y^2}{k^2}\right] E(k) = \frac{1}{2}(2 - \sin^2 \theta)E(k). \quad (77)$$

Due to two-dimensionalization of QS MHD flows, $\theta \approx \pi/2$. Hence

$$E_{\parallel} = E_{\perp} = E/2. \quad (78)$$

However, the numerical simulations of QS MHD turbulence exhibit very different behaviour, as will be shown in Sec. 6. Moreover, the velocity-velocity correlation tensor of QS MHD is anisotropic, hence it cannot be described by Eq. (71). See Sections 6.3.4 and 8 for further discussion.

Using Eqs. (76, 77), Sommeria and Moreau [64] (also see Knaepen and Moreau [28]) computed the ratio of the length scales parallel and perpendicular to the mean magnetic field as

$$\left(\frac{l_{\parallel}}{l_{\perp}}\right)^2 = \frac{\int d\mathbf{k}k_{\perp}^2 E(\mathbf{k})}{2 \int d\mathbf{k}k_{\parallel}^2 E(\mathbf{k})} = \frac{\int d\mathbf{k}(1 - \cos^2 \theta)E(\mathbf{k})}{2 \int d\mathbf{k}(\cos^2 \theta)E(\mathbf{k})}. \quad (79)$$

Using Eq. (74) and setting $\theta \approx \pi/2$, they argued that

$$\left(\frac{l_{\parallel}}{l_{\perp}}\right)^2 \approx \frac{1}{\langle \cos^2 \theta \rangle} \approx \frac{t}{t_J} \quad (80)$$

or

$$\frac{l_{\parallel}}{l_{\perp}} \sim \sqrt{\frac{t}{t_J}}. \quad (81)$$

Thus, l_{\parallel} elongates with time as $t^{1/2}$, and l_{\parallel}/l_{\perp} saturates at approximately one eddy turnover time. Hence using Eq. (35), Sommeria and Moreau [64] obtained

$$\frac{l_{\parallel}}{l_{\perp}} \sim \sqrt{N}. \quad (82)$$

Using dimensional analysis Sreenivasan and Alboussière [65, 66] derived the time evolution of QS MHD turbulence in the *nonlinear regime* under the assumption of conservation of total angular momentum. They obtained the following set of equations:

$$E^{1/2}l_{\perp}^2l_{\parallel}^{1/2} = \text{const}, \quad (83)$$

$$\frac{dE}{dt} \sim -\frac{E}{t_J} \left(\frac{l_{\perp}}{l_{\parallel}}\right)^2, \quad (84)$$

$$N_t = \frac{l_{\perp}^2l_{\parallel}^{1/2}}{t_J E^{1/2}} \left(\frac{l_{\perp}}{l_{\parallel}}\right)^2 \sim 1, \quad (85)$$

where N_t was called the *true interaction parameter* [65, 66]. The solutions of the above equations are

$$\frac{E}{E_0} \sim \left[1 + \frac{1}{N_0} \frac{t}{t_J}\right]^{-1}, \quad (86)$$

$$\frac{l_{\parallel}}{l_0} \sim N_0^{2/5} \left[1 + \frac{1}{N_0} \frac{t}{t_J} \right]^{3/5}, \quad (87)$$

$$\frac{l_{\perp}}{l_0} \sim N_0^{-1/10} \left[1 + \frac{1}{N_0} \frac{t}{t_J} \right]^{1/10}, \quad (88)$$

which yield $E \sim t^{-1}$ for large t , contrary to the Moffatt's decay law according to which $E \sim t^{-1/2}$ [see Eq. (75)]. Sreenivasan and Alboussière [66] argued that their decay law is similar to that of Alemany *et al* [1].

Experiments and numerical simulations of QS MHD show that the energy spectrum of the flow is steeper than 3D hydrodynamic turbulence, which is described by Kolmogorov's $k^{-5/3}$ spectrum. Kit and Tsinober [25], Kolesnikov and Tsinober [29], and Hossain [22] invoked 2D hydrodynamic turbulence phenomenology and argued that $E(k)$ is near k^{-3} due to two dimensionalization of the QS MHD turbulence. Verma and Reddy [74] however argued that the steepening of the energy spectrum is due to the loss of energy flux $\Pi(k)$ due to the Joule dissipation (to be detailed in Sec. 8). In a related work, Ishida and Kaneda [23] derived an expression for the velocity spectrum of QS MHD using perturbation method and showed that $E(k) \sim k^{-7/3}$.

The QS MHD flow is quasi two-dimensional with strong \mathbf{U}_{\perp} and small U_{\parallel} . Researchers have attempted to compute the energy exchange among \mathbf{U}_{\perp} and U_{\parallel} using various mechanisms. Thess and Zikanov [69] performed linear stability analysis of QS MHD in a triaxial ellipsoid and unbound QS MHD flows to model the transition from two-dimensional flows to three-dimensional flows. They observed that the two-dimensional flows become three-dimensional abruptly with a sudden burst. Klein and Pothérat [26] and Pothérat [53] proposed that *barrel effect* is responsible for the transformation of a quasi-2D flow to a 3D flow in wall-bounded geometries; here two-dimensional rotational currents play an important role. Favier *et al* [19, 20] and Reddy *et al* [57] argued that \mathbf{U}_{\perp} feeds energy to U_{\parallel} , thus making the flow quasi two-dimensional. Favier *et al* [20] performed EDQNM (Eddy-Damped Quasi-Normal Markovian) closure to QS MHD turbulence and found results similar to their numerical work [19]. It will be interesting to find detailed connections between the anisotropy mechanisms proposed by Thess and Zikanov [69], Klein and Pothérat [26], Favier *et al* [19], and Reddy *et al* [57].

The theoretical arguments described in the present section are inspired by several experiments. In addition, experiments have been performed to test some of the aforementioned turbulence models. We will describe some key experiments of QS MHD turbulence in the next section.

4. Experiments of QS MHD turbulence

In this section we will describe some of the leading experimental results on QS MHD turbulence. In all these experiments, a turbulent flow is subjected to an external magnetic field. Turbulence is typically provided by the interaction of the flow with a grid, as in laboratory experiments involving hydrodynamic turbulence. The velocity fluctuations are measured by potential probes. The frequency spectrum is computed

from the velocity time series, and the wavenumber spectrum $E(k)$ is interpolated from the frequency spectrum using Taylor's hypothesis [52].

Alemaný *et al* [1] performed an experiment in which turbulence is generated by a moving grid in a mercury column, and computed the energy spectrum for various interaction parameters. For small interaction parameters ($N < 3$), $E(k) \sim k^{-5/3}$, but for large interaction parameters, $E(k) \sim k^{-3}$. Alemany *et al* argued that the k^{-3} energy spectrum for large N is due to the quasi-equilibrium between the Joule dissipation and the angular energy transfers. They also showed that the decay rate of the kinetic energy follows $E(t) \sim t^{-1.7}$.

Branover *et al*'s [8] performed experiment on a mercury channel in the presence of a constant magnetic field. They generated turbulence in the flow using a honey-comb grid. For Branover *et al*, the range of N is 0.15–27 and that of the Hartman number (defined in Sec. 9) is 60–1200. They reported that for small interaction parameters ($N \sim 1$), the spectral index is approximately $-5/3$, but for moderate and large interaction parameters, the spectral exponents range from $-7/3$ to $-11/3$.

Eckert *et al* [18] studied the energy spectrum in a liquid sodium channel with turbulence enhancers to reduce the effects of M-profiles [47] in the flow. Between the Hartmann layers they observed quasi 2D vortices aligned along the external magnetic field. Eckert *et al* showed that the spectral exponent decreases from $-5/3$ to -5 as interaction parameter $N \in [0.3, 1000]$ is increased, as illustrated in Fig. 3(a). For very large N , the spectral exponent of approximately -5 is too steep, and it is better described by exponential spectrum, i.e. $E(k) \sim \exp(-ak)$, as indicated by Reddy *et al* [58]. In Fig. 3(b) we illustrate how the experimental $E(k)$ of Eckert *et al* for $N = 250$ is better described by an exponential spectrum than the power law spectrum. This issue will be revisited in Sections 5 and 8.

Kolesnikov and Tsinober [29], and Kit and Tsinober [25] performed experiment of QS MHD turbulence and observed steepening of the energy spectrum with the increase of N . They attribute the above feature to two-dimensionalization of the flow. Sreenivasan and Alboussière [66] performed an experiment on mercury in a channel subjected to a uniform external magnetic field. They reported that the duration of the initial *linear* decaying phase of the MHD flow increases with an increase of the interaction parameter. Klein and Pothérat [26] and Pothérat and Klein [54] performed QS MHD experiment to explore how the flow becomes three-dimensional. They showed that the inertia and two-dimensional rotational currents make the flow three-dimensional.

The liquid metal flows in engineering and planetary interiors typically involve walls that affect the flow due to the induced wall currents. However in this review we focus on flows where the effects of walls are negligible. This is to study the bulk properties of QS MHD turbulence away from the walls. In Sec. 9 we briefly describe the behaviour of QS MHD with walls, as well as pattern formation in a box containing liquid metal [63, 21].

In numerical simulations we observe similar features as above. We will describe them in the next section.

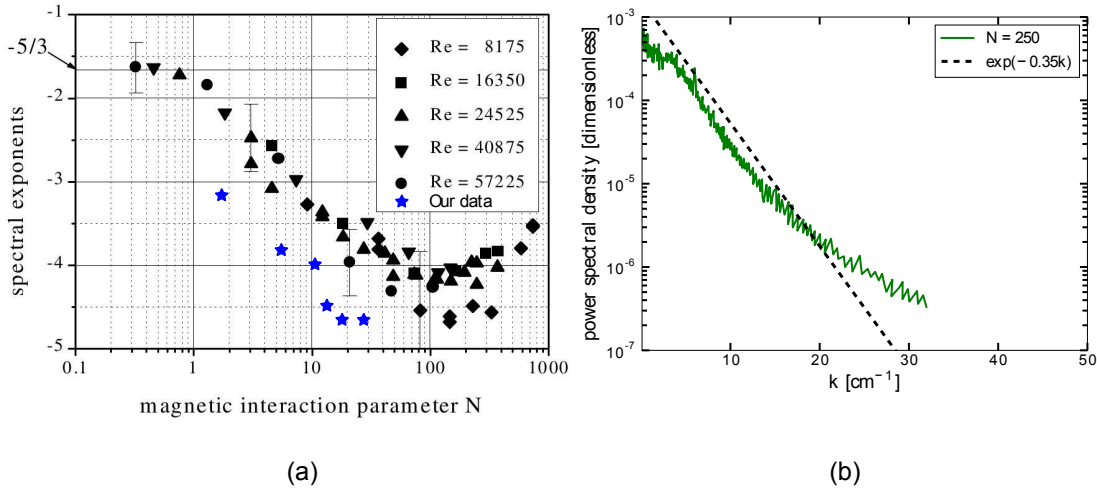


Figure 3. (a) A plot of the spectral exponents vs. N as reported by Eckert *et al* [18] in liquid-sodium experiment. (b) A plot of $E(k)$ vs. k for $N = 250$. Figure (a) is adopted from Eckert *et al* [18]. From Reddy *et al* [58]. Reprinted with permission from AIP Publishing.

5. Simulation of QS MHD turbulence

In this section, we will describe how QS MHD turbulence is simulated using computers. The equations of QS MHD are solved in a given volume for a given boundary condition and initial condition. The equations are solved in real space using the finite difference, finite volume, and finite element methods, or in Fourier space using the pseudo-spectral method.

Liquid metal flows in industrial applications and laboratory experiments involve complex geometries where the walls play important role. Such flows are best solved in real space using finite difference, finite volume, and finite element methods. Equations (31, 32, 33) are solved in this scheme. For a given boundary condition on ϕ , the Poisson's equation, Eq. (32), yields ϕ , which is used to compute \mathbf{J} . After this, Eq. (33) is used to solve for the velocity field. In this review we focus on bulk flows in QS MHD turbulence for which spectral method is more appropriate. Hence we do not discuss the finite difference, finite volume, and finite element methods in detail. Refer to Vantieghem *et al* [70] and references therein for details.

Often we try to understand the properties of the bulk flow by ignoring the boundary effects. For such studies, periodic boundary condition is employed, and the equations are solved conveniently using pseudo-spectral method. [This scheme also allows us to explore structures, energy, and anisotropy at different scales; this exploration is the main objective of the review.](#) Researchers have simulated QS MHD turbulence using pseudospectral method for various values of Re and N , and studied energy spectrum

and flux.

In a channel flow, to be discussed in 9 in somewhat more detail, typically no-slip boundary condition ($\mathbf{u} = 0$) is employed at the walls. Such systems are solved using finite difference, finite volume, finite element methods, or pseudospectral method with Chebyshev polynomials or other special basis functions satisfying no-slip boundary condition [17]. One example of Chebyshev implementation is by Boeck *et al* [5] who simulated low-Rm MHD flow in a channel with no-slip boundary conditions for Reynolds number of 8000. Note that the flows with very thin boundary layers (called Hartmann layer for QS MHD turbulence) are very expensive to compute using conventional spectral methods due to extreme resolution required to simulate the sharp velocity gradients in the Hartmann layer. The cost of such computation increases with the increase of Ha. Dymkou and Poth erat [17] overcame this difficulty by formulating a new basis function based on the least dissipative modes. Using this method Kornet and Poth erat [32] performed direct numerical simulations of MHD flows in a channel.

Here we present a short summary of the numerical results of QS MHD turbulence. In Secs. 6 and 7 we will report the anisotropic spectra and anisotropic energy transfers deduced using the numerical data obtained from spectral studies.

5.1. Quasi 2D nature of QS MHD flow

Numerical simulations (e.g. [22, 61, 79]) show that the QS MHD flow is nearly isotropic for small interactions N , but it is quasi 2D for large N . The degree of two-dimensionality increases with the increase of N . Schumann [61] simulated decaying QS MHD turbulence in a periodic box for N ranging from 0 to 50. For large N , he reported that the velocity fluctuations along B_0 are strongly suppressed, and the flow becomes quasi 2D. Zikanov and Thess [79] performed forced simulations and observed that the flow remains three-dimensional and turbulent for a low interaction parameter ($N \approx 0.1$), but becomes quasi-two-dimensional with sporadic bursts for a moderate interaction parameter ($N \approx 0.4$), and purely quasi-2D for a high interaction parameter ($N \approx 10$). Burattini *et al* [9] and Vorobev *et al* [77] studied anisotropy of QS MHD turbulence. Vorobev *et al* [77] quantified the flow anisotropy and showed that for $N = 5$, $E_{\perp}(k)/E_{\parallel}(k) > 1$ at low wavenumbers, and $E_{\perp}(k)/E_{\parallel}(k) < 1$ at higher wavenumbers. We will details these results in Sec. 6.

Favier *et al* [19] performed simulation of decaying QS MHD for N ranging from 1 to 5 and studied anisotropy. They showed that the flow is two-dimensional with three-components (2D-3C). Later, Reddy and Verma [58], and Reddy *et al* [57] performed spectral simulations of forced QS MHD turbulence for N from 0 to 220 and observed similar behaviour. We illustrate these features using several flow profiles. In Fig. 4 we illustrate the isocontours of the vorticity field for $N = 0, 5.5$, and 18, with \mathbf{B}_0 along \hat{z} , and in Fig. 5 we show the velocity vector for $N = 18$ and 130. The flow is isotropic for $N = 0$, but it starts to become anisotropic as N takes larger values. For $N = 18$ and 130, the flows have strong $\mathbf{U}_{\perp} = U_x\hat{x} + U_y\hat{y}$ and weak $U_{\parallel} = U_z$. Clearly the flow is not

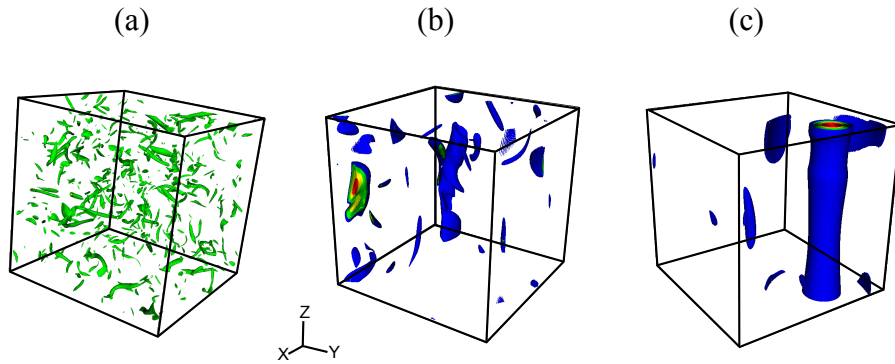


Figure 4. Isosurfaces of the absolute value of vorticity, $|\nabla \times \mathbf{u}|$, for (a) $N = 0$ (isotropic), (b) $N = 5.5$, and (c) $N = 18$. The flow field is anisotropic for $N \neq 0$. From Reddy *et al* [58]. Reprinted with permission from AIP Publishing.

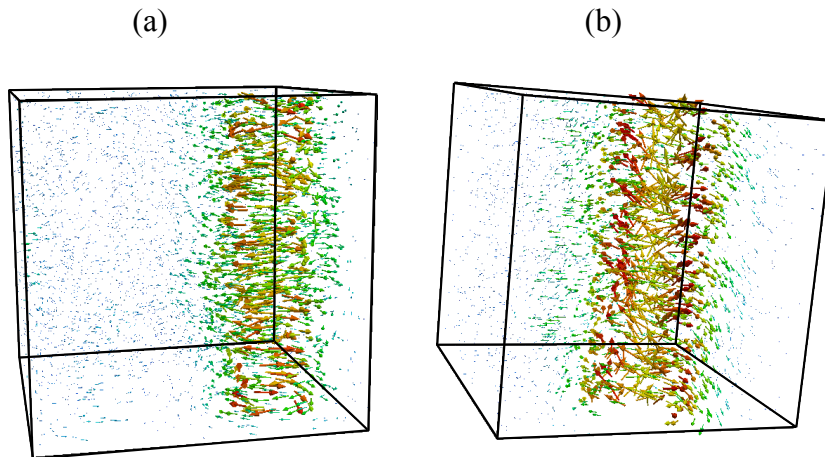


Figure 5. Plot of the velocity field for (a) $N = 18$ and (b) $N = 130$ exhibiting quasi 2D flow. U_z For $N = 130$ is stronger than that for $N = 18$. From Reddy *et al* [58]. Reprinted with permission from AIP Publishing.

two-dimensional, but quasi two-dimensional, or two-dimensional with three-components (2D-3C) [19, 58]. For $N = 132$, the strength of U_z is larger than that for $N = 18$, as shown in Fig. 5. In later sections we will investigate how the anisotropy changes with N , and explore the reasons for the quasi-2D nature of QS MHD turbulence.

Another important aspect of spectral simulation is the quantification of energy spectrum, which is described in the next subsection.

5.2. One-dimensional energy spectrum

Most spectral works report one-dimensional energy spectrum $E(k)$ which is defined using Eq. (51). The aforementioned one-dimensional energy spectrum describes the average

energy in a shell. This is useful since it describes the energy contents at different scales. It also helps us contrast QS MHD turbulence with isotropic hydrodynamic turbulence.

As described in Sec. 2.5, for 3D hydrodynamic turbulence ($N = 0$), $E(k) \sim \Pi^{2/3} k^{-5/3}$ [see Eq. (68)]. However for 2D hydrodynamic turbulence, $E(k) \sim \Pi^{2/3} k^{-5/3}$ for $k < k_f$ and $E(k) \sim \Pi_\omega^{2/3} k^{-3}$ for $k > k_f$, where k_f is the forcing wavenumber band, and Π_ω is the enstrophy flux. The numerical results described in the present section and the experiments results of Sec. 4 reveal that $E(k)$ is steeper than Kolmogorov's $k^{-5/3}$ power law, but it also differs from 2D hydrodynamic turbulence. Understanding $E(k)$ of QS MHD turbulence is one of the major topics of this review.

Using numerical simulations, Hossain [22] showed that for low interaction parameters N (~ 0.1), the flow is three-dimensional and it exhibits a forward cascade of energy (from small wavenumbers to higher wavenumbers). However, for large ($N = 10$), he reported that $E(k) \sim k^{-3}$, and related it to 2D hydrodynamic turbulence [34]. Ishihara *et al* [24] employed tensorial and dimensional analysis to compute anisotropic corrections in a turbulent shear flow, and showed that the velocity correlation function can be approximated as

$$Q_{ij}(\mathbf{k}) = \frac{K_{\text{Ko}}}{4\pi k^2} \Pi^{2/3} k^{-5/3} P_{ij}(\mathbf{k}) + Q_{ij}^{(1)}(\mathbf{k}), \quad (89)$$

where Π is the energy flux, $P_{ij}(\mathbf{k}) = \delta_{ij} - k_i k_j / k^2$, and $Q_{ij}^{(1)}(\mathbf{k})$ is the anisotropic tensor. Ishihara *et al* [24] modelled $Q_{ij}^{(1)}(\mathbf{k})$ as

$$Q_{ij}^{(1)}(\mathbf{k}) = C_{ij\alpha\beta} S_{\alpha\beta}, \quad (90)$$

where $S_{\alpha\beta}$ is the traceless tensor representing the shear stress, and

$$C_{ij\alpha\beta} = \frac{E_{as}(k)}{4\pi k^2} (P_{i\alpha}(\mathbf{k}) P_{j\beta}(\mathbf{k}) + P_{i\beta}(\mathbf{k}) P_{j\alpha}(\mathbf{k})) + \frac{E_{bs}(k)}{4\pi k^2} \frac{k_\alpha k_\beta}{k^2} \quad (91)$$

with

$$E_{as}(k) = A \Pi^{1/3} k^{-7/3}, \quad (92)$$

$$E_{bs}(k) = B \Pi^{1/3} k^{-7/3}, \quad (93)$$

where A, B are constants. Ishida and Kaneda [23] extended Ishihara *et al*'s arguments to QS MHD turbulence and computed the modification in the inertial-range energy spectrum for low interaction parameters. They showed that for low interaction parameters, $E(k) \sim k^{-7/3}$, in similar lines as the results of Ishihara *et al* [24]; Ishida and Kaneda [23] confirmed this result with direct numerical simulations. Burattini *et al* [10] studied the nonlinear energy transfers and the energy flux using numerical simulations for $N = 0, 1$ and 5. They observed that the anisotropic energy spectra are proportional to $k^{-7/3}$ for $N = 0$ and 1 (see Fig. 6(a)), consistent with the predictions of Ishida and Kaneda [23]. They also observed that for large N , $E(k)$ is steeper than $k^{-7/3}$ (see Fig. 6(b)). Vorobev *et al* [77] performed direct numerical simulations and large-eddy simulations of QS MHD turbulence and showed that the spectral exponent varies for $-5/3$ to -3 as N is increased from 0 to 5. In Fig. 7, we illustrate $E(k)$ of Vorobev *et al*'s DNS.

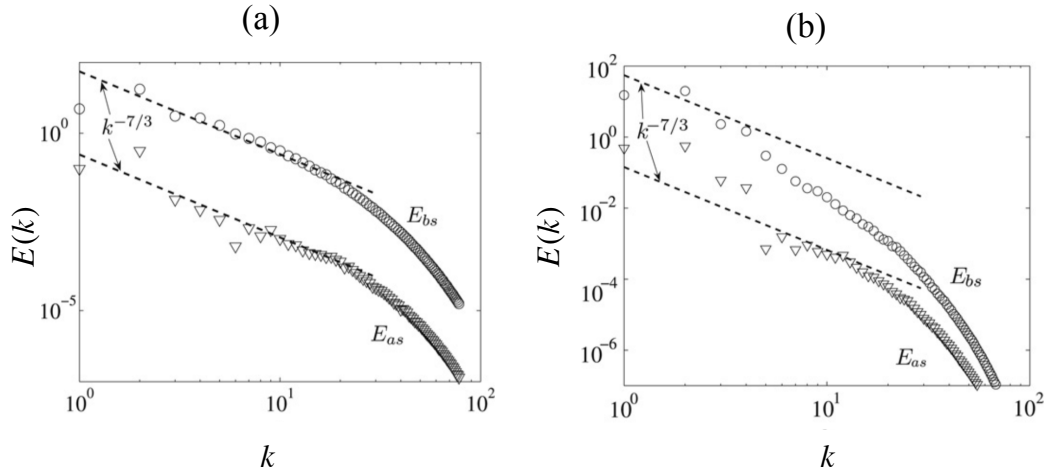


Figure 6. Anisotropic energy spectrum $E_{as}(k)$ and $E_{bs}(k)$ reported by Burattini *et al* [10] for (a) $N = 1$ and (b) $N = 5$. $E(k) \sim k^{-7/3}$ for $N = 1$, but it is steeper than $k^{-7/3}$ for $N = 5$. The definitions of $E_{as}(k)$ and $E_{bs}(k)$ are given by Eqs. (92,93) respectively. From Burattini *et al* [10]. Reprinted with permission from Elsevier.

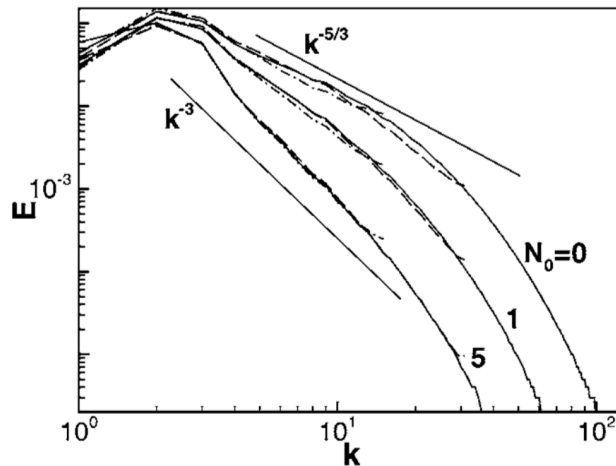


Figure 7. In the forced QS MHD turbulence simulation of Vorobeve *et al* [77], steepening of the energy spectrum $E(k)$ as the interaction parameter N is increased from 0 to 5. From Vorobeve *et al* [77]. Reprinted with permission from AIP Publishing.

Many researchers [29, 25, 22] attribute the aforementioned steepening of the energy spectrum to two-dimensionalization. Note that two-dimensional hydrodynamic turbulence has $E(k) \sim k^{-3}$ for large k [34]. Verma and Reddy [74] however argue that the steepening of $E(k)$ in QS MHD turbulence occurs due to the Joule dissipation. According to Eq. (55), in QS MHD turbulence, the Joule term dissipates kinetic energy at all scales, hence the flux $\Pi(k)$ decreases with wavenumber k , unlike constant $\Pi(k)$ in the inertial range of hydrodynamic turbulence. As a result, $E(k)$ of QS MHD turbulence

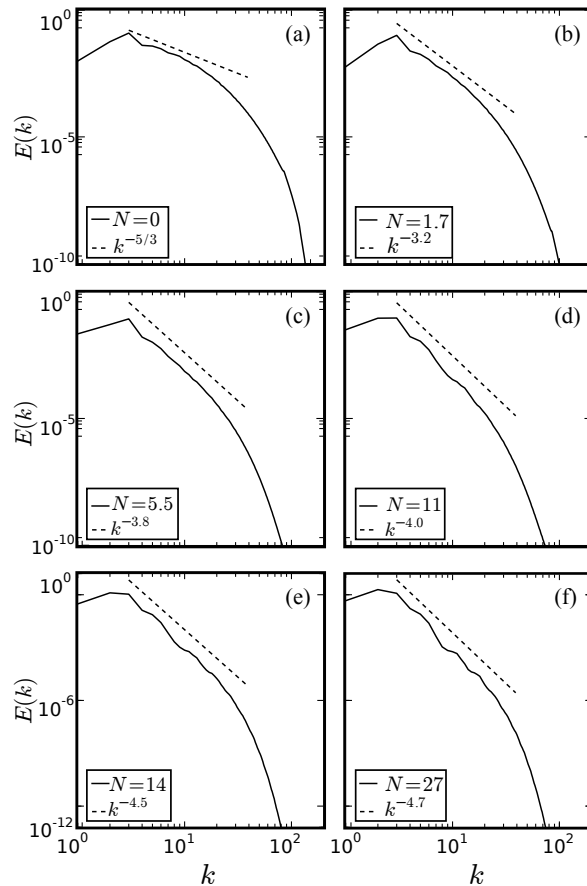


Figure 8. Kinetic energy spectra for (a) $N = 0$, (b) $N = 1.7$, (c) $N = 5.5$, (d) $N = 11$, (e) $N = 14$, and (f) $N = 27$. In the inertial range $E(k) \sim k^{-\alpha}$ with the spectral indices $\alpha = 5/3, 3.2, 3.8, 4.0, 4.5, 4.7$ respectively. Reprinted with permission from Reddy [56].

is steeper than the hydrodynamic $k^{-5/3}$ spectrum. In Figs. 8(a-f) and Fig. 9, we exhibit the energy spectra reported by Reddy and Verma [58] for $N = 0, 1.7, 5.5, 11, 14, 27, 130$ and 220 . These spectra are for the statistical steady-state data of forced run (forcing applied at $k_f = 1$ to 3). For $N = 0, 1.7, 5.5, 11, 14, 27$, $E(k) \sim k^{-\alpha}$ with the spectral indices $\alpha = 5/3, 3.2, 3.8, 4.0, 4.5, 4.7$ respectively. But for $N = 130$ and 220 , the spectrum follows exponential behaviour— $\exp(-0.18k)$ and $\exp(-0.19k)$ respectively. The errors in the coefficients are of the order of 10%. These results are summarised in Table 2. The decrease of the energy flux $\Pi(k)$ with k leads to the aforementioned steepening of the energy spectrum.

5.3. Miscellaneous numerical results of QS MHD turbulence

Thess and Zikanov [69] performed linear stability analysis to study the flow transition from 2D to 3D. They performed their study for inviscid flows in a triaxial ellipsoid and observed that the two-dimensional flows abruptly become three-dimensional with a sudden burst. In another development, for low-Rm flows, Poth erat et al [55] observed

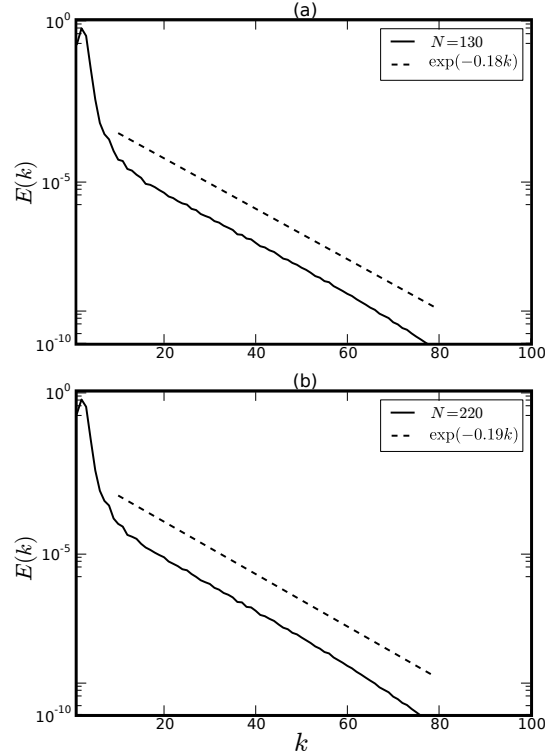


Figure 9. Kinetic energy spectra for (a) $N = 130$ and (b) $N = 220$ (very large values of N) that exhibit $E(k) \sim \exp(-0.18k)$ and $\exp(-0.19k)$ respectively. Reprinted with permission from Reddy [56].

Table 2. Parameters of the simulation: the grid size, the interaction parameter N computed at the steady state, the interaction parameter N_0 computed at the instant when external magnetic field is applied, the integral length scale L , the anisotropy ratio $A = E_{\perp}/2E_{\parallel}$, the ratio of the Joule dissipation and the viscous dissipation $\epsilon_J/\epsilon_{\nu}$, and the spectral laws.

Grid	N	N_0	L	$A = E_{\perp}/2E_{\parallel}$	$\epsilon_J/\epsilon_{\nu}$	spectral law
256^3	0	0	0.095	1.0	0	$k^{-5/3}$
512^3	0	0	0.096	0.99	0	$k^{-5/3}$
512^3	0.1	0.1	0.095	1.01	0.28	$k^{-1.8}$
512^3	0.64	0.5	0.105	1.01	2.07	$k^{-2.0}$
512^3	1.6	1.0	0.11	1.05	4.4	$k^{-2.8}$
256^3	1.7	1.0	0.12	1.1	4.2	$k^{-3.2}$
256^3	5.5	2.5	0.14	1.5	9.7	$k^{-3.8}$
256^3	11	5.0	0.15	4.5	11	$k^{-4.0}$
256^3	14	7.5	0.15	8.0	11	$k^{-4.5}$
256^3	18	10.0	0.15	16	9.8	$k^{-4.7}$
256^3	27	20.0	0.15	1.6	6.9	$k^{-4.7}$
256^3	130	—	0.17	3.0	4.1	$\exp(-0.18k)$
256^3	220	—	0.17	1.7	3.9	$\exp(-0.19k)$

three-dimensionalization of quasi-two-dimensional quasi-static MHD flows due to the *barrel effect* [53]. In a channel flow, Boeck *et al* [5] also observed recurring transitions between two-dimensional and three-dimensional states. In decaying QS MHD flows, Burattini *et al* [11] reported $t^{-1/2}$ decay law for the kinetic energy.

There have been simulations of MHD turbulence at low magnetic Reynolds number. Knaepen *et al* [27] showed that the behaviour of low-Rm MHD is similar to QS MHD turbulence ($\text{Rm} \rightarrow 0$). We also remark that the quasi 2D nature and steepening of $E(k)$ of QS MHD turbulence observed in numerical simulations are consistent with similar findings in experiments discussed in Sec. 4.

In the next section we will describe angular distribution of energy in Fourier space.

6. Anisotropic energy distribution in QS MHD turbulence

Quantification of anisotropy in turbulent flow is a challenge. For two-dimensional magnetohydrodynamic turbulence, Shebalin *et al* [62] proposed a measure of anisotropy for any quantity Q as

$$\theta_Q = \tan^{-1} \frac{k_z^2 Q(\mathbf{k})}{k_x^2 Q(\mathbf{k})} \quad (94)$$

that can be easily generalised to three dimensions. Researchers [10, 19, 60, 68] decomposed the Fourier space into rings and quantified the energy contents in rings as *ring spectrum*. For a more detailed measure, some researchers have studied the energy contents in toroidal and poloidal components of a vector field [19, 60]. We also remark that spherical harmonics have been used to quantify anisotropy [3].

In QS MHD, a strong external magnetic field B_0 induces Joule dissipation $NE(k)\cos^2\theta$ that is dependent on the polar angle θ (see Fig. 1(b)). Consequently, the energy distribution in QS MHD is anisotropic, in contrast to the hydrodynamic turbulence for which the energy distribution is isotropic in the inertial range. Zikanov and Thess [79] reported the energy contents of the perpendicular and parallel components of the velocity field. Vorobev *et al* [77] showed that for $N = 5$, $E_\perp(k)/E_\parallel(k) > 1$ at low wavenumbers, and $E_\perp(k)/E_\parallel(k) < 1$ at higher wavenumbers.

Burattini *et al* [9, 10] computed the ring spectrum, as well as the energy spectra of the perpendicular and components of velocity. Favier *et al* [19, 20] quantified anisotropy in QS MHD turbulence using the toroidal and poloidal components of the velocity field. Recently Reddy and Verma [58] studied the ratio $E_\perp/(2E_\parallel)$, ring spectrum, Joule dissipation spectrum etc. Their analysis is for a wide range of N —from 0 to 220. In the following discussion, we will summarise the results on the anisotropy in QS MHD turbulence.

6.1. Anisotropy of total energy and dissipation rates of QS MHD turbulence

Reddy and Verma [58] quantified the anisotropy of the total energy using an anisotropic parameter

$$A = \frac{E_{\perp}}{2E_{\parallel}} \quad (95)$$

where $E_{\perp} = (U_x^2 + U_y^2)/2$ and $E_{\parallel} = U_z^2/2$. In Table 2 we list the values of A as well as $\epsilon_J/\epsilon_{\nu}$ under steady state of the forced turbulence runs. By definition, for isotropic flows ($N = 0$), $A = 1$. The flow continues to be nearly isotropic till $N = 1.7$ for which $A \approx 1.1$. Beyond $N = 1.7$, A increases with N till $N = 18$ after which it decreases with the increase of N . These observations show that the flow is quasi 2D for large N , consistent with the illustrations of Figs. 4 and 5. In the following discussion, we demonstrate that in QS MHD turbulence, the energy dissipates more strongly in the polar region than in the equatorial region due to the $\cos^2\theta$ term of Eq. (45). The two-dimensionalisation of QS MHD further strengthens U_{\perp} due to the inverse cascade of kinetic energy.

The maximum value of $E_{\perp}/(2E_{\parallel})$ occurs at $N \approx 18$. This is due to the fact that the strength of U_{\perp} increases with N until $N \approx 18$. However for $N > 18$, U_{\perp} transfers energy to U_{\parallel} via pressure thus making E_{\parallel} significant. This feature is evident in Fig. 5 where U_{\parallel} is stronger for $N = 130$ than for $N = 18$. Interestingly, the ratio of the Joule dissipation rate ϵ_J and the viscous dissipation rate ϵ_{ν} also peaks near $N \approx 14$. For $N > 0.64$, ϵ_J dominates ϵ_{ν} because the large-scale velocity is dissipated more effectively by ϵ_J than ϵ_{ν} . In addition, for very large N , the increased strength of E_{\parallel} makes ϵ_{ν} significant. We revisit these connections in Sec. 6.3.2.

6.2. Anisotropy in energy spectrum in QS MHD turbulence

To explore the nature of the anisotropy at different length scales, a wavenumber-dependent anisotropy measure, $E_{\perp}(k)/2E_{\parallel}(k)$, has been proposed [9, 58, 77]. The ratio plotted in Fig. 10 shows that $E_{\perp}(k) > E_{\parallel}(k)$ at low wavenumbers, which is due to the inverse cascade of U_{\perp} at small k . The ratio $E_{\perp}(k)/2E_{\parallel}(k)$ increases with N upto $N = 18$, after which it decreases. The occurrence of peak at $N \approx 18$ is due to energy transfer from U_{\perp} to U_{\parallel} for $N > 18$, as discussed in previous subsection.

For large wavenumbers, the ratio $E_{\perp}(k)/2E_{\parallel}(k)$ is near unity till $N = 18$, after which it decreases monotonically with N [19, 58, 77]. For large N , the significant increase of $E_{\parallel}(k)$ at large k is due to the energy transfer from U_{\perp} to U_{\parallel} , and subsequent forward cascade of U_{\parallel} . These observations lend strong credence to the observed 2D-3C nature of QS MHD turbulence, first proposed by Favier *et al* [19]. We will demonstrate these energy exchanges in Sec. 7.

Further insights into the anisotropy and angular dependence of the energy distribution in the spectral space are obtained by the ring spectrum, which will be discussed below.

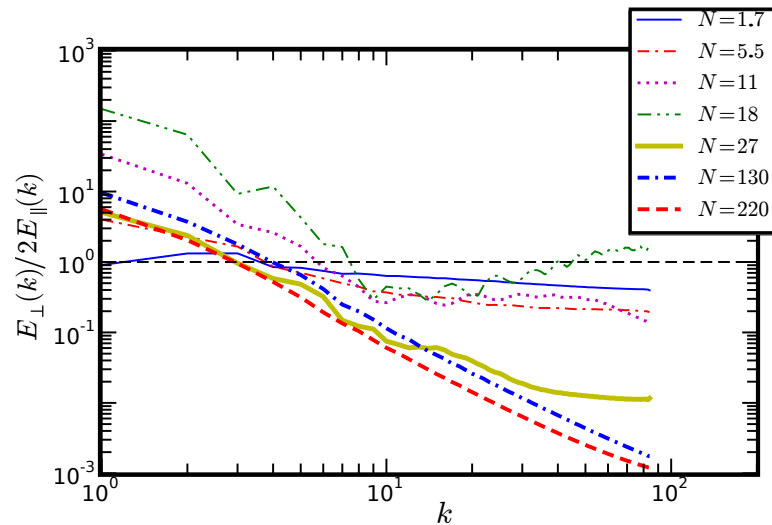


Figure 10. Variation of $A = E_{\perp}(k)/2E_{\parallel}(k)$ with k for various values of the interaction parameter N . From Reddy and Verma [58]. Reprinted with permission from AIP Publishing.

6.3. Angular dependence of energy spectrum in QS MHD turbulence

Researchers have devised measures to quantify the angular dependence of $E(\mathbf{k})$ in QS MHD turbulence. In the following discussion, we list four measures: the angular variation of the energy of the toroidal and poloidal components of the velocity field (see Sec. 2.3 and Fig. 2 for definition); ring spectrum; decomposition of the ring spectrum using Legendre polynomials; and tensorial representation.

6.3.1. Toroidal and Poloidal decomposition Favier *et al* [19] divided the Fourier space into 5 angular regions (rings) of equal angular widths, and computed the cumulative energy contents of the toroidal and Poloidal components in these rings (see Sec. 2.3 and Fig. 2). They performed two decaying QS MHD simulations for $N = 1$ and 5 and computed the toroidal and poloidal angular energy spectra, which are denoted by $E^{\text{tor}}(k)$ and $E^{\text{pol}}(k)$. In Fig. 11, $E^{\text{tor}}(k)$ and $E^{\text{pol}}(k)$ are represented using solid and dotted lines respectively. The plots show that the energy of QS MHD turbulence is concentrated near the equator. The energy contents in the polar region is much smaller than that in the equatorial region.

6.3.2. Ring spectrum for QS MHD turbulence A given wavenumber shell is divided into rings which are indexed using shell index m and sector index α (see Figures 12 for an illustration) [9, 10, 58]. A ring is an intersection of a shell and a sector [68]. This scheme is similar to that of Favier *et al* [19]; they chose 5 sectors in their decomposition. Note that the mean magnetic field is aligned along $\theta = 0$. Also, the average $E(\mathbf{k})$ of QS MHD turbulence is independent of the azimuthal angle ϕ , hence $E(\mathbf{k})$ is function only of k and θ .

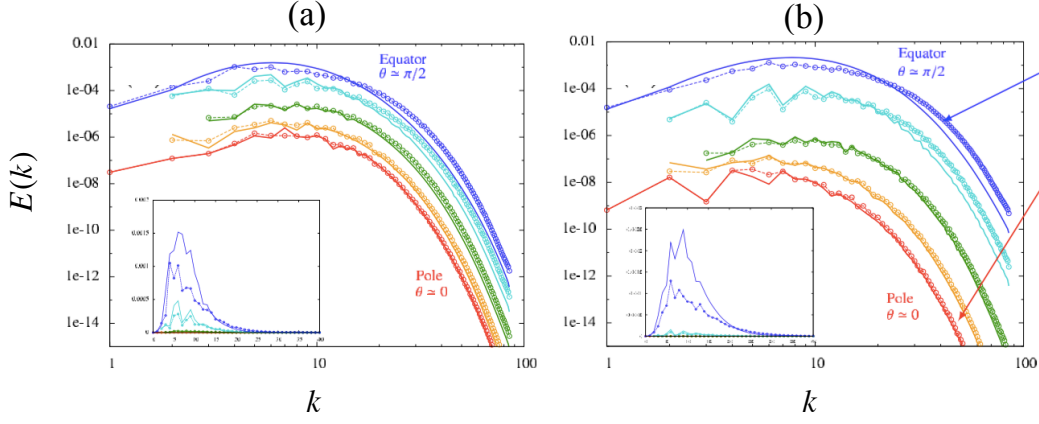


Figure 11. Angular energy spectra $E^{\text{tor}}(k)$ (solid line) and $E^{\text{pol}}(k)$ (dotted lines) of the five angular rings from the pole (red curve) to the equator (blue curve): (a) for $N = 1$ at $t = 5t_J$, and (b) for $N = 5$ at $t = 20t_J$, where $t_J = \eta/B_0^2$ is the diffusive time due to the Lorentz force. The embedded figure represent the same plots in linear scale. From Favier *et al* [19]. Reprinted with permission from AIP Publishing.

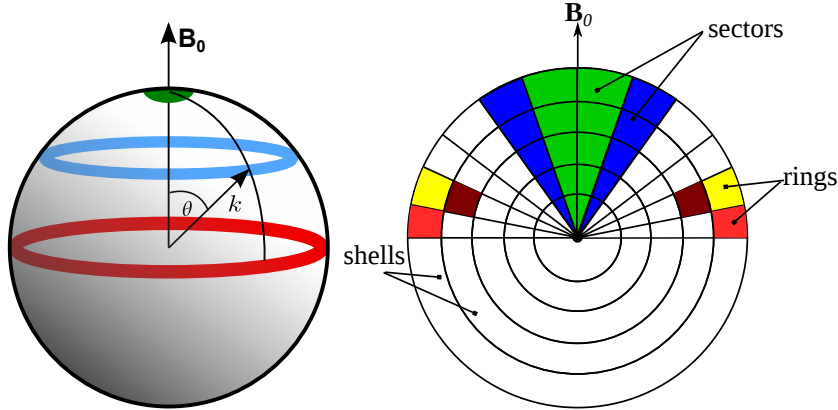


Figure 12. (a) Illustration of the ring decomposition in the spectral space. (b) A cross-sectional view of the wavenumber shells, sectors, and rings.

The ring spectrum $E(k, \theta)$ is defined as

$$E(k, \theta) = \frac{1}{C_\alpha} \sum_{k \leq |\mathbf{k}'| < k+1; \angle(\mathbf{k}') \in [\theta_\alpha, \theta_{\alpha+1})} \frac{1}{2} |\mathbf{U}(\mathbf{k}')|^2, \quad (96)$$

where $\angle(\mathbf{k}')$ is the angle between \mathbf{k}' and \mathbf{B}_0 , and α is the index of the sector whose angular range is from θ_α to $\theta_{\alpha+1}$. Reddy and Verma [58] divided the sum with a normalization factor

$$C_\alpha = |\cos(\theta_\alpha) - \cos(\theta_{\alpha+1})| \quad (97)$$

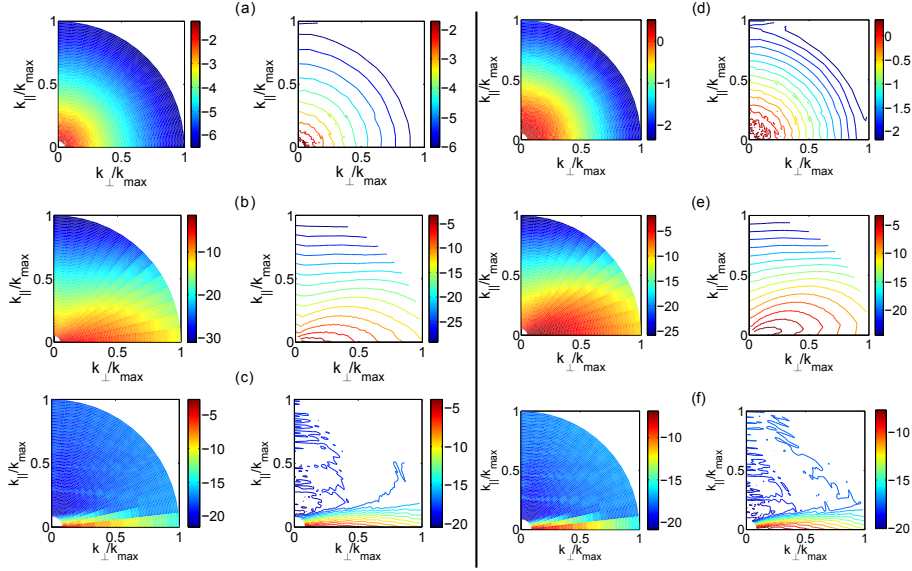


Figure 13. Angular distribution of the logarithm of the kinetic energy ($\log(E(k, \theta))$) for (a) $N = 0$, (b) $N = 18$ and (c) $N = 130$ exhibited as density and contour plots. The corresponding angular distribution of the Joule dissipation rate ($\log(\epsilon_J(k, \theta))$) for (d) $N = 0$, (e) $N = 18$, and (f) $N = 130$. Reprinted with permission from Reddy [56].

to compensate for the effects of a larger number of modes in the rings with larger θ . This factor is related to the $d \cos \theta$ factor in the volume integral in spherical geometry. After normalization, $E(k, \theta)$ is a measure of the average energy per mode in a given ring. A corollary, for a given k in an isotropic flow, the ring spectra of all the rings are equal in a statistical sense.

Burattini *et al* [9] plotted three-dimensional $E(k_x, k_y, k_z)$ of QS MHD turbulence and showed that the energy is suppressed along the z direction. Note that the ring spectrum averages the energy in the $k_x k_y$ plane for a given k_z by exploiting the azimuthal symmetry.

Reddy and Verma [58] divided the spectral space in the northern hemisphere into thin shells of unit widths. The shells in turn were further divided into 15 thin rings from $\theta = 0$ to $\theta = \pi/2$ with sector widths of $\pi/30$. Note that the southern hemisphere has the same ring spectrum as the northern hemisphere due to $\theta \rightarrow \pi - \theta$ symmetry, hence we compute the energy spectrum only for the northern hemisphere. Figure 13(a,b,c) exhibits the density and contour plots of the energy spectrum $E(k, \theta)$ for $N = 0, 18$, and 130 respectively [58]. The energy spectrum for $N = 0$ is isotropic, but those for $N = 18$ and 130 are anisotropic, with the degree of anisotropy increasing with N . Since the viscous dissipation rate $\epsilon_\nu(k, \theta) \propto E(k, \theta)$, $\epsilon_\nu(k, \theta)$ has the same distribution as $E(k, \theta)$. However, the Joule dissipation rate $\epsilon_J(k, \theta) = 2B_0'^2 E(k, \theta) \cos^2 \theta$ has an additional $\cos^2 \theta$ dependence. As a result, $\epsilon_J(k, \theta)$ does not peak at $\theta = \pi/2$, but before $\theta = \pi/2$. In Fig. 13(d,e,f) we exhibit the $\epsilon_J(k, \theta)$ that exhibits the above properties for $N = 0, 18, 130$

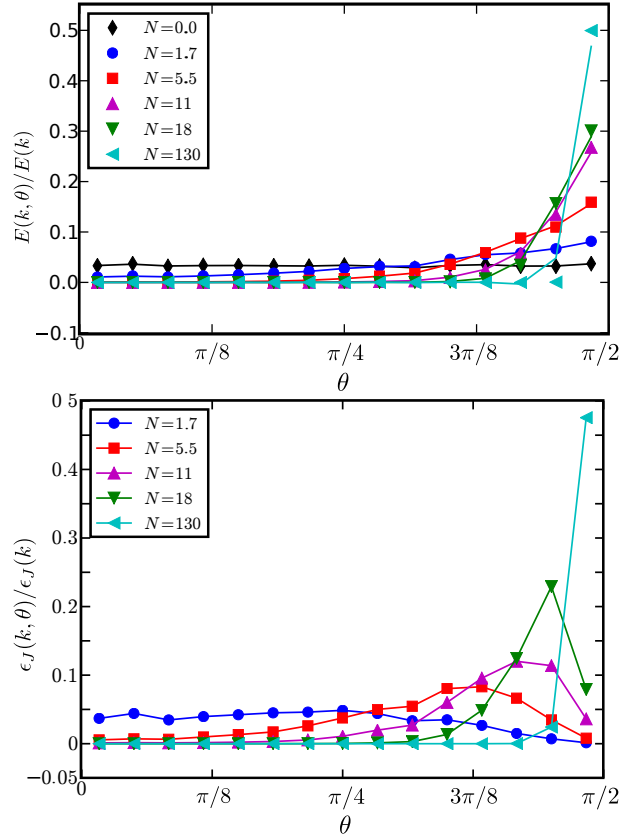


Figure 14. For various N : (a) Plot of $E(k = 20, \theta)/E(k = 20)$ vs. θ . (b) Plot of the normalized Joule dissipation rate $\epsilon_J(k = 20, \theta)/\epsilon_J(k = 20)$. From Reddy and Verma [58]. Reprinted with permission from AIP Publishing.

respectively [56].

The ring spectra demonstrates that the flow is strongly anisotropic for large N with strong concentration of energy near $k_{\parallel} \approx 0$ plane. Using the information of Figs. 10 and 13(a,b,c) we conclude that low wavenumber modes have significant \mathbf{U}_{\perp} , but the intermediate and large wavenumber modes have dominant U_z [58]. This feature is consistent with the real-space profile shown in Figs. 4 and 5. In Fig. 14 we exhibit the normalised ring spectrum $E(k = 20, \theta)/E(k = 20)$ and $\epsilon_J(k = 20, \theta)/\epsilon_J(k = 20)$ that confirms the above behaviour.

The Lorentz force vanishes at $\theta = \pi/2$ due to the $\cos^2 \theta$ factor, hence the nonlinear term $\mathbf{U} \cdot \nabla \mathbf{U}$ dominate in the $k_z = 0$ plane. Therefore QS MHD turbulence has behaviour similar to 2D hydrodynamics in the $k_z = 0$ plane. These observations yield dynamical perspectives to the findings of earlier researchers [1, 10, 18, 25, 29, 46] who reported that QS MHD turbulence exhibits behaviour similar to 2D hydrodynamics.

The ratio of the angular distribution of the dissipation rates is given by [57]

$$\frac{\epsilon_{\nu}(k, \theta)}{\epsilon_J(k, \theta)} = \frac{2\nu'k^2 E(\mathbf{k})}{2B_0^2 \cos^2 \theta E(\mathbf{k})} = \frac{2\nu'k^2}{2B_0^2 \cos^2 \theta}. \quad (98)$$

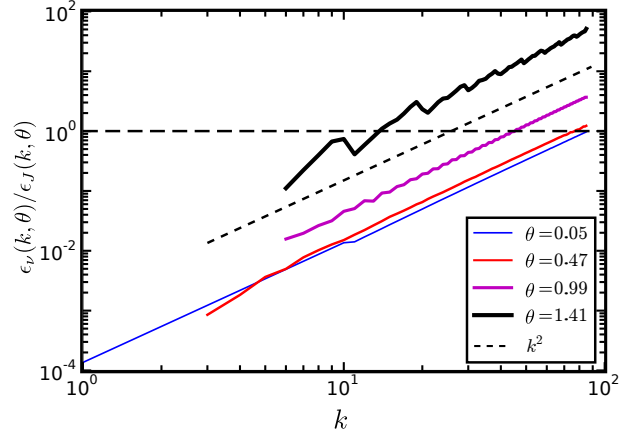


Figure 15. For $N = 27$, $\epsilon_\nu(k, \theta)/\epsilon_J(k, \theta)$ vs. k for various sectors. $\epsilon_\nu(k, \theta)/\epsilon_J(k, \theta) \sim k^2$. From Reddy *et al* [57]. Reprinted with permission from AIP Publishing.

Thus, $\epsilon_\nu(k, \theta) = \epsilon_J(k, \theta)$ at

$$k^* = \frac{B'_0 \cos \theta}{\sqrt{\nu'}}. \quad (99)$$

Hence $\epsilon_J(k, \theta) > \epsilon_\nu(k, \theta)$ for $k < k^*$, consistent with the fact that ϵ_J dominates at low wavenumbers. For a sector of angle θ , the ratio $\epsilon_\nu(k, \theta)/\epsilon_J(k, \theta) \propto k^2$. In Fig. 16 we plot the Joule dissipation spectrum [56]

$$\epsilon_J(k) = \int 2B_0'^2 \cos^2 \theta E(k, \theta) d\theta \quad (100)$$

and the viscous dissipation

$$\epsilon_\nu(k) = 2\nu' k^2 E(k). \quad (101)$$

Clearly the Joule dissipation dominates at small wavenumbers, while the viscous dissipation at large wavenumbers.

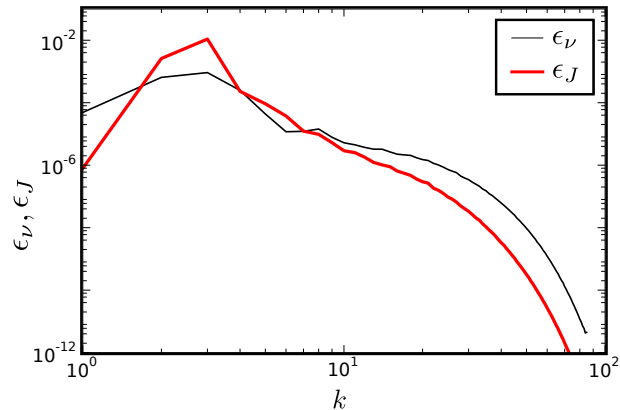


Figure 16. The Joule dissipation spectrum ϵ_J and viscous dissipation spectrum ϵ_ν for $N = 27$. Reprinted with permission from Reddy [56].

6.3.3. *Anisotropy quantification using Legendre polynomials* Isotropic systems typically exhibit spherically symmetric correlations. For example, we expect $E(k, \theta)$ of isotropic and homogeneous turbulence to be independent of θ . However, induction of external magnetic field or rotation breaks the spherical symmetry, and $E(k, \theta)$ becomes function of both k and θ . Note however that the angular anisotropy could be scale-dependent, that is, the system may exhibit variations at different angular resolutions. Such multi-resolution variations are not easily quantifiable using $E(k, \theta)$, but they are easier to quantify using polynomials. For such analysis, it is customary to employ spherical harmonics, which are also eigenfunctions of the Laplacian operator (∇^2). This analysis is analogous to the Fourier transform in which the Fourier amplitudes for various k 's capture the scale-dependent features of the system.

QS MHD turbulence under the influence of a constant external magnetic field is azimuthally symmetric, hence the energy spectrum $E(\mathbf{k})$ is independent of ϕ . Reddy and Verma [58] exploited this symmetry and employed Legendre polynomials to extract the angular dependence of the ring spectrum as

$$E(k, \theta) = \sum_l a_l P_l(\cos \zeta), \quad (102)$$

where the angle $\zeta = \pi/2 - \theta$ is chosen so as to keep the maximum of the function at $\zeta = 0$. The coefficient a_0 represents the isotropic component of the flow or $E(k, \theta)$, while higher a_l 's provide information about the anisotropic components. Note that odd-indexed a_l 's are negligible due to the $\theta \rightarrow \pi - \theta$ symmetry.

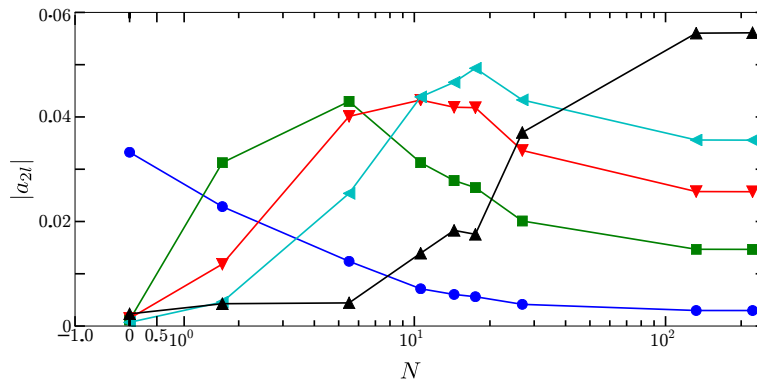


Figure 17. The coefficients a_l of the Legendre polynomials of Eq. (102) for $N \in [0, 220]$, $k = 20$. Here a_0 : filled-circle (blue), a_2 : ■ (green), a_4 : ▼ (red), a_6 : ◄ (turquoise), and a_{16} : ▲ (black). From Reddy and Verma [58]. Reprinted with permission from AIP Publishing.

Reddy and Verma [58] computed a_{2l} using the numerical ring spectrum, $E(k, \theta)$; the results are exhibited in Fig. 17. For $N = 0$, a_0 dominates all other modes. As exhibited in the figure, the amplitudes of a_2 , a_4 , a_6 , and a_{16} are most significant for $N = 5.5, 11, 18$, and 220 respectively. Thus, larger N have maximum amplitude at larger l . This observation is consistent with the fact that the peak of the ring spectrum

$E(k, \theta)$ shifts towards the equatorial region ($\theta \rightarrow \pi/2$) as N increases. See Figs. 13 and 14 for comparison.

It is important to note that for spherically symmetric systems, the solution of the equations may not satisfy the spherical symmetry. A well-known example is the Hydrogen atom; here the potential $V(\mathbf{r}) = -1/r$ is spherically symmetric, but all the wavefunctions of the electrons are not spherically symmetric. In similar lines, it has been shown that the correlation function of the hydrodynamic turbulence contains anisotropic tensorial components in its expansion [3, 36]. Note that in the QS MHD turbulence, the external mean magnetic field breaks the isotropy of the system as well as that of its equation. Thus, the degree of anisotropy in QS MHD is much larger than that in isotropic fluid turbulence, and the spherical harmonics are useful tools to specify the anisotropy. We expect the anisotropy in QS MHD turbulence to be much stronger than that in the hydrodynamic turbulence.

6.3.4. Tensorial representation of anisotropy Researchers have also attempted to express the velocity correlation function using tensors. One such attempt is by Verma [71] who proposed a formula for the correlation function in the presence of an external field along \hat{n} as

$$\langle \hat{u}_i(\mathbf{k}) \hat{u}_j^*(\mathbf{k}) \rangle = \phi_{ij}(\mathbf{k}, t) = \left(\delta_{ij} - \frac{k_i k_j}{k^2} \right) C_1(k) + P'_{ij}(\mathbf{k}, \mathbf{n}) C_2(k), \quad (103)$$

where

$$P'_{ij}(\mathbf{k}, \mathbf{n}) = \left(n_i - \frac{\mathbf{n} \cdot \mathbf{k}}{k^2} k_i \right) \left(n_j - \frac{\mathbf{n} \cdot \mathbf{k}}{k^2} k_j \right). \quad (104)$$

Here $C_1(k), C_2(k)$ are scalar functions of k . From the above expressions, the modal energy is

$$\frac{1}{2} \langle |\hat{\mathbf{u}}(\mathbf{k})|^2 \rangle = C_1(k) + \frac{1}{2} \sin^2 \theta C_2(k), \quad (105)$$

where $\hat{n} \cdot \hat{k} = \cos \theta$. The above expression for the modal energy uses only $P_0(\cos \zeta)$ and $P_2(\cos \zeta)$, hence Eq. (103) cannot describe the velocity correlations for moderate and large N that involves higher P_l 's, as evident from Eq. (102) and Fig. 17.

Ishida and Kaneda [23] employed perturbation method to derive a tensorial representation for the correlation function of QS MHD turbulence for small N ; their arguments are based on symmetries. Note that the formula of Ishida and Kaneda [23] too is not applicable for general N . Hence, general tensorial expression for the energy spectrum needs to be expanded using Eq. (102). Note that Eq. (71) of Sec. 3, which is a special case of Eq. (103) with $C_2 = 0$, is also inapplicable for strongly anisotropic QS MHD turbulence.

In this section we showed that for large N , the kinetic energy is concentrated near the equator. We also observed that the E_{\perp}/E_{\parallel} peaks around $N \approx 18$ due to interesting exchange of energy between U_{\parallel} and \mathbf{U}_{\perp} . We will investigate these energy transfers in the next section, and explore further reasons for the quasi 2D behaviour of QS MHD turbulence.

7. Energy Transfers in QS MHD turbulence

The nonlinear interactions among the Fourier modes of Eq. (40) yield energy transfers among the modes of QS MHD. A major effort in turbulent research is how to quantify these transfers. Kraichnan [33] computed the energy transferred to one of the modes in a wavenumber triad $(\mathbf{k}, \mathbf{p}, \mathbf{q})$ that satisfied $\mathbf{k} = \mathbf{p} + \mathbf{q}$. Later, Dar *et al* [12] and Verma [71] developed a formalism in which the energy transfer rate from mode \mathbf{p} to mode \mathbf{k} with mode \mathbf{q} as a mediator is

$$S(\mathbf{k}|\mathbf{p}|\mathbf{q}) = \Im\{[\mathbf{k} \cdot \hat{\mathbf{U}}(\mathbf{q})][\hat{\mathbf{U}}^*(\mathbf{k}) \cdot \hat{\mathbf{U}}(\mathbf{p})]\}, \quad (106)$$

where \Im is the imaginary part. Reddy *et al* [57] used the above formula to compute the energy flux, shell-to-shell energy transfers, and ring-to-ring energy transfers in QS MHD turbulence. We will discuss these measures in the present section.

7.1. Cumulative measures: Energy flux for QS MHD turbulence

The energy flux $\Pi(k_0)$ is defined as the energy transferred from the modes residing inside a sphere of wavenumber radius k_0 to the modes outside the same sphere [33, 38, 71], which is

$$\Pi(k_0) = \sum_{|\mathbf{k}| > k_0} \sum_{|\mathbf{p}| \leq k_0} S(\mathbf{k}|\mathbf{p}|\mathbf{q}). \quad (107)$$

Using the statistical steady-state data of forced QS MHD turbulence, Reddy *et al* [57] computed the energy flux for $N = 1.7, 5.5, 11, 27, 130$ and 220 , some of which are plotted in Fig. 18. These plots are for the random forcing at $k_f = (1, 3)$. For the hydrodynamic case ($N = 0$), the energy flux is an approximate constant in the inertial range, which is consistent with the classical Kolmogorov flux [30, 31]. For $N > 0$, the Joule dissipation at different scales leads to a decrease of $\Pi(k)$ with k as $d\Pi(k)/dk = -(\epsilon_\nu(k) + \epsilon_J(k))$ [see Eq. (55)]. The decay of the energy flux leads to steepening of the energy spectrum, as discussed in Sec. 5.2, and as shown in Figs. 7, 8, and 9. In Sec. 8.1 we will review the models that capture the variations of the kinetic energy flux in the presence of Joule dissipation. According to these models, $\Pi(k) \sim k^{-a}$ for small and moderate N 's, and $\Pi(k) \sim \exp(-ak)$ for large N 's ($N \geq 130$).

Figure 18 does not capture an important aspect of QS MHD turbulence. The Lorentz force, which is proportional to $B_0'^2 \cos^2 \theta$, vanishes at $\theta = \pi/2$. Hence, in $k_z = 0$ plane, the nonlinear term $\mathbf{u} \cdot \nabla \mathbf{u}$ is the most effective term for large Re , and the flow has behaviour similar to 2D hydrodynamic turbulence with an inverse cascade of energy at wavenumbers lower than the forcing wavenumber band k_f . For the runs described above, $k_f = (1, 3)$, hence the energy flux does not exhibit inverse cascade. However, the small wavenumbers ($k \sim 1$) do receive energy due to nonlinearity, because of which $E_\perp/E_\parallel \gg 1$ for small k , as shown in Fig. 10. The inverse energy transfers lead to quasi 2D flow structures of Figs. 4 and 5.

To explore the nature of the inverse energy cascade in QS MHD turbulence, Reddy *et al* [57] simulated forced QS MHD for $N = 100$ with the forcing wavenumber band

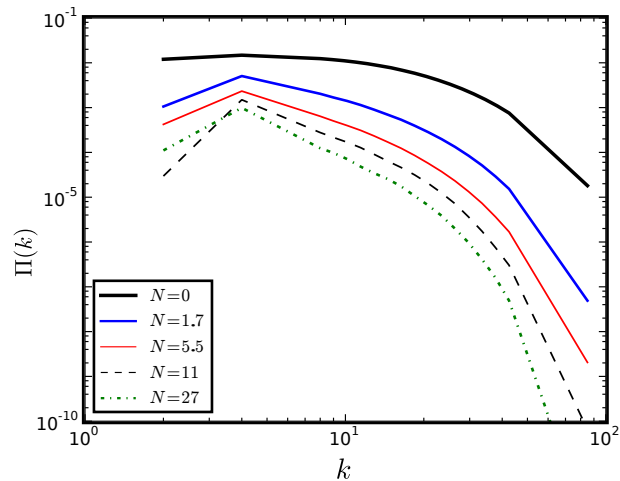


Figure 18. Kinetic energy flux $\Pi(k)$ for $N = 0, 1.7, 5.5, 11,$ and 27 for $k_f = (1, 3)$. Reprinted with permission from Reddy [56].

$k_f = (8, 9)$. Figure 19 illustrates the energy spectra of the parallel and perpendicular components of the velocity field for this simulation. Here $E_{\perp}(k) \gg 2E_{\parallel}(k)$ for $k < k_f$, but $2E_{\parallel}(k) \gg E_{\perp}(k)$ for $k > k_f$. Also, for $k < k_f$, $E_{\perp}(k) \sim k^{-5/3}$, thus exhibiting behaviour similar to 2D hydrodynamic turbulence.

Reddy *et al* [57] computed the energy flux $\Pi(k)$ (for $k_f = (8, 9)$) which is exhibited in Fig. 20 as a dashed curve. We observe a negative $\Pi(k)$ for $k < k_f$, thus demonstrating an inverse cascade of kinetic energy. However $\Pi(k) > 0$ for $k > k_f$ indicating a forward energy cascade in this range. Note that 2D hydrodynamic turbulence predicts $\Pi(k) \approx 0$ for $k > k_f$ [6]. The above observation that $\Pi(k) > 0$ for $k > k_f$, a major deviation from 2D hydrodynamics, is due to the forward cascade of U_{\parallel} . The dominance of E_{\parallel} over E_{\perp} for $k > k_f$ (Fig. 19) is due to this flux. We will compute the fluxes of \mathbf{U}_{\perp} and U_{\parallel} in Sec. 7.4.

The energy flux is a cumulative energy transfer from the modes inside a wavenumber sphere to the modes outside the sphere. The shell-to-shell energy transfers, to be described in the next section, provides a more detailed picture of the energy transfer in turbulence.

7.2. Shell-to-shell energy transfers of QS MHD turbulence

The shell-to-shell energy transfer rate is another quantity used for quantifying the energy transfers. The shell-to-shell energy transfer rate from all the modes of shell m to the modes of shell n is defined as

$$T_n^m = \sum_{\mathbf{k} \in n} \sum_{\mathbf{p} \in m} S(\mathbf{k}|\mathbf{p}|\mathbf{q}), \quad (108)$$

where $S(\mathbf{k}|\mathbf{p}|\mathbf{q})$ is given by Eq. (106). For hydrodynamics turbulence, T_n^m has been shown to be local and forward in the inertial range, i.e., the maximal energy transfer takes place from shell m to $m + 1$ [15, 38, 39, 73].

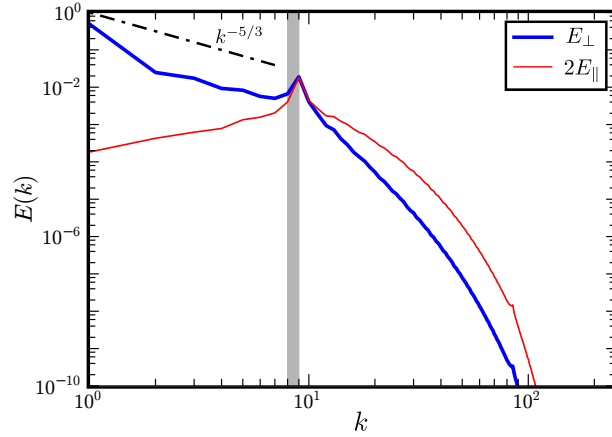


Figure 19. Plots of $E_{\perp}(k)$ and $2E_{\parallel}(k)$ for $N = 100$ when $k_f \in [8, 9]$ (the shaded region). For $k < k_f$, $E_{\perp}(k) > E_{\parallel}(k)$ with $E_{\perp}(k) \sim k^{-5/3}$, but for $k > k_f$, $E_{\perp}(k) < E_{\parallel}(k)$. From Reddy *et al* [58]. Reprinted with permission from AIP Publishing.

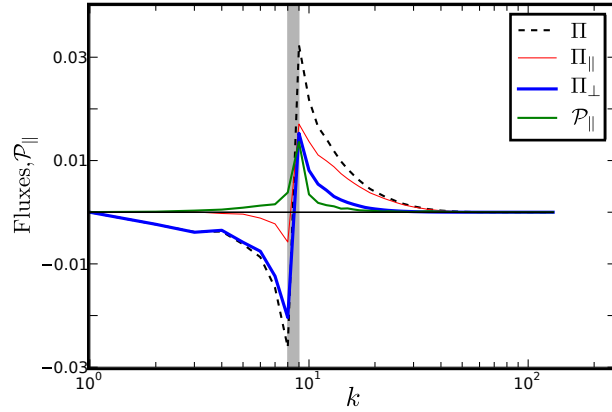


Figure 20. Plots of the energy fluxes $\Pi(k)$, $\Pi_{\parallel}(k)$, $\Pi_{\perp}(k)$ and $\mathcal{P}_{\parallel}(k)$ for $N = 100$ when $k_f \in [8, 9]$ (the shaded region). For $k < k_f$, $\Pi_{\perp}(k) < 0$ indicating an inverse cascade for \mathbf{U}_{\perp} , while for $k > k_f$, $\Pi_{\parallel}(k) > 0$ exhibiting a forward cascade for U_{\parallel} . $\mathcal{P}_{\parallel}(k) > 0$ for $k > k_f$, indicating an energy transfer from \mathbf{U}_{\perp} to U_{\parallel} via pressure. From Reddy *et al* [57]. Reprinted with permission from AIP Publishing.

Reddy *et al* [57] computed the shell-to-shell energy transfers for QS MHD turbulence when $k_f = (1, 3)$. They binned the Fourier space logarithmically with the shell radii as 4.0, 8.0, 8.9, 9.9, 10.9, 12.2, 13.5, 14.9, 16.6, 18.4, 20.5, 22.7, 25.2, 28.0, 31.1, 34.5, 38.3, 42.5, and 85.0. Figure 21 exhibits the shell-to-shell energy transfer rates for $N = 1.7, 11, 18$, and 130. The figure shows that shell n gives energy to shell $(n + l)$ with $(l > 0)$, and it receives energy from shell $(n - l)$ indicating forward energy transfer. Also, the maximum energy transfer is to the nearest neighbour, i.e., shell n gives the maximum positive energy transfer to the shell $(n + 1)$. Therefore we conclude that the shell-to-shell energy transfer in QS MHD turbulence is local and forward.

The shell-to-shell transfers are dominant for small m and n , specially for large N .

This is because the energy dominantly resides in small wavenumber shells. This feature differs from 3D hydrodynamic turbulence for which the shell-to-shell energy transfer is local for a larger range of wavenumbers. Also, for $k < k_f$ we expect a backward energy transfer. This feature of QS MHD needs to be investigated for large k_f .

The energy flux and the shell-to-shell energy transfers provide an averaged measure over the polar angle θ of Fig. 12, hence they do not capture the anisotropic energy transfers which are θ -dependent. In the following, we present the ring-to-ring energy transfers using which we can quantify θ -dependent anisotropic energy transfers.

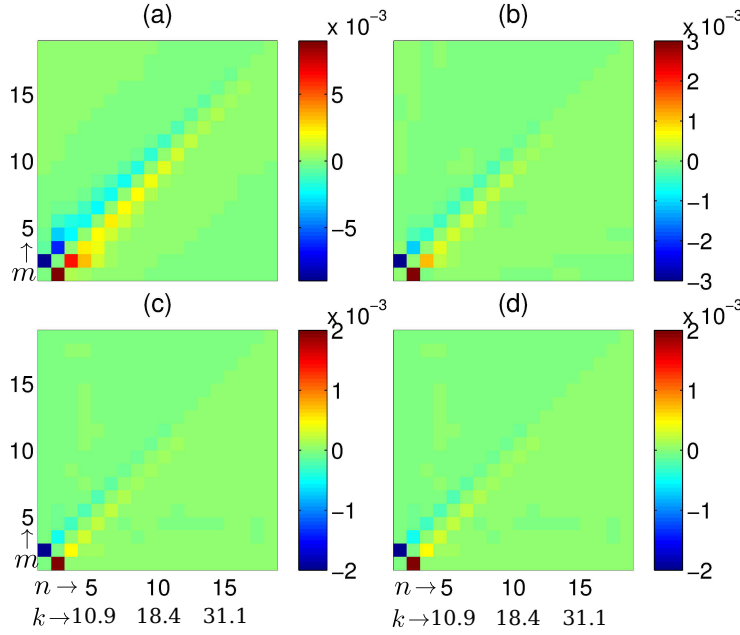


Figure 21. Forward and local shell-to-shell energy transfer rates T_n^m for (a) $N = 1.7$, (b) $N = 11$, (c) $N = 18$, and (d) $N = 130$. *Notation* m : giver shell, n : receiver shells, k the wavenumber of the outer radius of the corresponding shell. From Reddy *et al* [57]. Reprinted with permission from AIP Publishing.

7.3. Anisotropic measures: Ring-to-ring energy transfers of QS MHD turbulence

Reddy *et al* [57] divided the wavenumber shells into rings, as shown in Figure 12. The ring-to-ring energy transfer rate from the ring (m, α) to the ring (n, β) is [68]

$$T_{(n,\beta)}^{(m,\alpha)} = \sum_{\mathbf{k} \in (n,\beta)} \sum_{\mathbf{p} \in (m,\alpha)} S(\mathbf{k}|\mathbf{p}|\mathbf{q}), \quad (109)$$

where $S(\mathbf{k}|\mathbf{p}|\mathbf{q})$ is given by Eq. (106). The ring-to-ring energy transfers are normalized using $A_\alpha = |\cos(\theta_\alpha) - \cos(\theta_{\alpha+1})|$ to compensate for the uneven distribution of modes among the rings [68]; the rings closer to the equator have more Fourier modes than those near the poles. Therefore, the normalized ring transfer is

$$\overline{T}_{(n,\beta)}^{(m,\alpha)} = \frac{1}{A_\alpha A_\beta} T_{(n,\beta)}^{(m,\alpha)}. \quad (110)$$

Teaca *et al* [68] performed first such computations for MHD turbulence.

Reddy *et al* [57] computed the ring-to-ring energy transfers for $N = 1.7, 11, 18,$ and 130 using the steady-state numerical data. They observed that the maximum energy transfer takes place among the neighbouring rings (nearest shells and sectors), thus the energy transfers among the rings is local. In the following discussion, we focus on ring-to-ring transfers among the neighbouring shells, in particular, for the 9th and 10th shells. In Figs. 22 we present the results on the normalized ring-to-ring energy transfers $\overline{T}_{(n,\beta)}^{(m,\alpha)}$ from the rings of 9th shell ($m = 9$) to the rings of shells $n = 9$ and 10 . In these figures, the vertical axis represents the sector indices of the giver rings (α), while the horizontal axis represents the sector indices of the receiver rings (β).

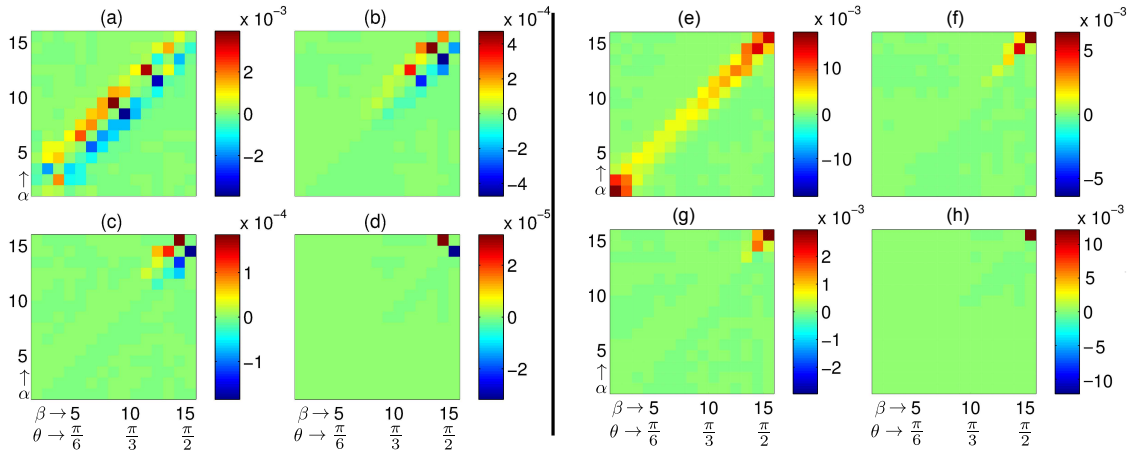


Figure 22. Ring-to-ring energy transfers $\overline{T}_{(9,\beta)}^{(9,\alpha)}$ among the rings of the 9th shell for (a) $N = 1.7$, (b) $N = 11$, (c) $N = 18$, and (d) $N = 130$; and $\overline{T}_{(10,\beta)}^{(9,\alpha)}$ for (e) $N = 1.7$, (f) $N = 11$, (g) $N = 18$, and (h) $N = 130$. *Notation* α : giver ring, β : receiver ring, θ : the angle of the corresponding rings. $\overline{T}_{(9,\beta)}^{(9,\alpha)}$ is dominant for neighbouring rings (local). For large N , the ring transfers are dominant near the equator. Figure (a) from Reddy *et al* [57]; reprinted with permission from AIP Publishing. Figure (b) reprinted with permission from Reddy [56].

According to Fig. 22(a-d), $\overline{T}_{(9,\beta)}^{(9,\alpha)}$ (the energy transfers among the rings within the 9th shell) has maximum value for $\overline{T}_{(9,\alpha\pm 1)}^{(9,\alpha)}$ with $\overline{T}_{(9,\alpha-1)}^{(9,\alpha)} > 0$ and $\overline{T}_{(9,\alpha+1)}^{(9,\alpha)} < 0$. Thus the energy transfer is local among the rings, and they are from larger θ to smaller θ . Hence, the energy transfer is local in the angular direction as well (along with the local shell-to-shell transfers described in the previous subsection). Another important feature of the ring-to-ring transfers is that for large N ($N = 11, 18, 130$), the dominant energy transfers takes place from the rings closer to the equator to their neighbours (lower θ). Thus, for large N , the dominant energy transfers take place near the equatorial region because the energy is concentrated near this region.

Figure 22(e-h) illustrates $\overline{T}_{(10,\beta)}^{(9,\alpha)}$, the energy transfers from the rings in the 9th

shell to those in the 10th shell (immediate neighbour of shell 9). The figure shows that $\overline{T}_{(10,\beta)}^{(9,\alpha)} > 0$ for all rings with the maximal transfers occurring for the equatorial rings ($\alpha, \beta \approx 15$). Using these observations, we conclude that the energy is transferred dominantly along a sector near the equator, and that the energy transfers are from lower k to larger k .

We summarise the ring-to-ring energy transfers in QS MHD using a schematic diagram exhibited in Fig. 23. The ring-to-ring transfers are local and forward along k , but local and inverse along θ (transfers from larger θ to smaller θ). For large N , these transfers tend to be dominant near the equator because the energy is concentrated near the equator. The energy transfer from larger θ to smaller θ is due to the stronger Joule dissipation at lower θ because of the $\cos^2 \theta$ factor.

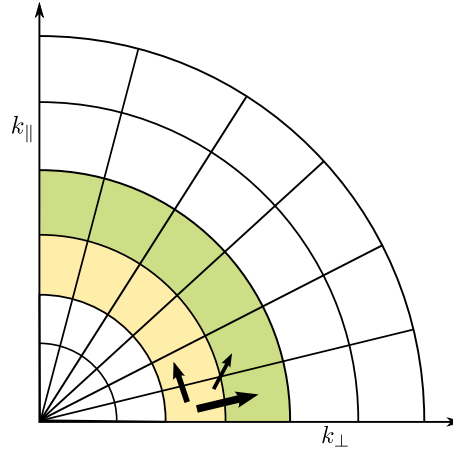


Figure 23. A schematic diagram exhibiting the dominant ring-to-ring energy transfers. The thickness of the lines is proportional to the intensity of the transfer. Figure (b) reprinted with permission from Reddy [56].

In an earlier discussions we had argued that U_{\perp} feeds energy to U_{\parallel} for large k 's. In the following subsection we will compute these transfers.

7.4. Energy transfers among the parallel and perpendicular components in QS MHD turbulence

The energy equations for the perpendicular and parallel components of the velocity field of QS MHD turbulence are [57]

$$\begin{aligned} \frac{\partial E_{\perp}(\mathbf{k})}{\partial t} &= \sum_{\mathbf{p}} S_{\perp}(\mathbf{k}|\mathbf{p}|\mathbf{q}) - 2B_0'^2 \cos^2(\theta) E_{\perp}(\mathbf{k}) + \mathcal{P}_{\perp}(\mathbf{k}) \\ &\quad - 2\nu' k^2 E_{\perp}(\mathbf{k}) + \Re\{\hat{\mathbf{F}}_{\perp}(\mathbf{k}) \cdot \hat{\mathbf{U}}_{\perp}^*(\mathbf{k})\}, \end{aligned} \quad (111)$$

$$\begin{aligned} \frac{\partial E_{\parallel}(\mathbf{k})}{\partial t} &= \sum_{\mathbf{p}} S_{\parallel}(\mathbf{k}|\mathbf{p}|\mathbf{q}) - 2B_0'^2 \cos^2(\theta) E_{\parallel}(\mathbf{k}) + \mathcal{P}_{\parallel}(\mathbf{k}) \\ &\quad - 2\nu' k^2 E_{\parallel}(\mathbf{k}) + \Re\{\hat{F}_{\parallel}(k) \hat{U}_{\parallel}^*(k)\}, \end{aligned} \quad (112)$$

where $\mathbf{q} = \mathbf{k} - \mathbf{p}$, $E_{\perp}(\mathbf{k}) = \frac{1}{2}|\hat{\mathbf{U}}_{\perp}(\mathbf{k})|^2$, $E_{\parallel}(\mathbf{k}) = \frac{1}{2}|\hat{U}_{\parallel}(\mathbf{k})|^2$, and

$$\mathcal{P}_{\perp}(\mathbf{k}) = \Im\{[\mathbf{k} \cdot \hat{\mathbf{U}}_{\perp}^*(\mathbf{k})]\hat{P}(\mathbf{k})\}, \quad (113)$$

$$\mathcal{P}_{\parallel}(\mathbf{k}) = \Im\{[k_{\parallel}\hat{U}_{\parallel}^*(\mathbf{k})]\hat{P}(\mathbf{k}')\}, \quad (114)$$

where $\hat{P}(\mathbf{k})$ is Fourier transform of the pressure field P .

Reddy *et al* [57] showed that \mathbf{U}_{\perp} Fourier modes exchange energy among themselves (see [Appendix A](#)). The energy transfer rate from $\mathbf{U}_{\perp}(\mathbf{p})$ to $\mathbf{U}_{\perp}(\mathbf{k})$ with $\mathbf{U}(\mathbf{q})$ acting as a mediator is given by

$$S_{\perp}(\mathbf{k}|\mathbf{p}|\mathbf{q}) = \Im\{[\mathbf{k} \cdot \hat{\mathbf{U}}(\mathbf{q})][\hat{\mathbf{U}}_{\perp}^*(\mathbf{k}) \cdot \hat{\mathbf{U}}_{\perp}(\mathbf{p})]\}, \quad (115)$$

while the energy transfer rate from $U_{\parallel}(\mathbf{p})$ to $U_{\parallel}(\mathbf{k})$ with $\mathbf{U}(\mathbf{q})$ acting as a mediator is given by

$$S_{\parallel}(\mathbf{k}|\mathbf{p}|\mathbf{q}) = \Im\{[\mathbf{k} \cdot \hat{\mathbf{U}}(\mathbf{q})][\hat{U}_{\parallel}^*(\mathbf{k})\hat{U}_{\parallel}(\mathbf{p})]\}. \quad (116)$$

The energy fluxes, $\Pi_{\perp}(k_0)$ and $\Pi_{\parallel}(k_0)$, of the perpendicular and parallel components of the velocity field can be defined using $S_{\perp}(\mathbf{k}|\mathbf{p}|\mathbf{q})$ and $S_{\parallel}(\mathbf{k}|\mathbf{p}|\mathbf{q})$. They are respectively the energy transfer rates of \mathbf{U}_{\perp} and U_{\parallel} out of the wavenumber sphere of radius k_0 :

$$\Pi_{\perp}(k_0) = \sum_{|\mathbf{k}|>k_0} \sum_{|\mathbf{p}|\leq k_0} S_{\perp}(\mathbf{k}|\mathbf{p}|\mathbf{q}), \quad (117)$$

$$\Pi_{\parallel}(k_0) = \sum_{|\mathbf{k}|>k_0} \sum_{|\mathbf{p}|\leq k_0} S_{\parallel}(\mathbf{k}|\mathbf{p}|\mathbf{q}). \quad (118)$$

Note that the total energy flux $\Pi(k_0) = \Pi_{\perp}(k_0) + \Pi_{\parallel}(k_0)$.

The energy equations (111, 112) reveal that \mathbf{U}_{\perp} and U_{\parallel} receive energy from the pressure as given by Eqs. (113) and (114). A closer inspection of Eqs. (113, 114) indicates that

$$\mathcal{P}_{\perp}(\mathbf{k}) + \mathcal{P}_{\parallel}(\mathbf{k}) = 0 \quad (119)$$

due to the incompressibility condition $\mathbf{k} \cdot \mathbf{u}(\mathbf{k}) = 0$. Thus, the pressure acts as a mediator for the energy transfer between \mathbf{U}_{\perp} and U_{\parallel} (see [Appendix A](#)). The parallel component U_{\parallel} receives energy from \mathbf{U}_{\perp} via pressure by an amount $\mathcal{P}_{\parallel}(\mathbf{k})$. We also remark that there is no direct energy exchange between \mathbf{U}_{\perp} and U_{\parallel} in the energy equation; and that the energy transfer via pressure is internal to a given mode. Also note that the pressure does not transfer energy from a mode \mathbf{p} to \mathbf{k} . Another consequence of the above results is that $\Pi_{\parallel}(k)$ and $\Pi_{\perp}(k)$ vary with k due to the energy exchange among themselves via pressure.

Reddy *et al* [57] computed $\Pi_{\parallel}(k)$, $\Pi_{\perp}(k)$, and $\mathcal{P}_{\parallel}(\mathbf{k})$ using the numerical data for the QS MHD run with $N = 100$ and $k_f = (8, 9)$. The results illustrated in [Fig. 20](#) show that in the $k < k_f$ region, Π_{\perp} , which is negative, dominates other fluxes; this is consistent with the inverse cascade of \mathbf{U}_{\perp} . In the $k > k_f$ region, Π_{\parallel} dominates Π_{\perp} , and it is positive indicating a forward cascade for U_{\parallel} [19, 20, 57]. The energy transfer from \mathbf{U}_{\perp} to U_{\parallel} via pressure is the reason for quasi 2D nature of QS MHD turbulence described earlier. Note that \mathbf{U}_{\perp} is primarily dissipated by the Joule heating since it is

active at small k , while U_{\parallel} is dissipated by the viscous force due to its dominance at large k (see Figs. 15 and 16).

The above phenomena along with its physical interpretation can be summarised as follows. Equation (112) shows that U_{\parallel} receives energy from \mathbf{U}_{\perp} via pressure, and the rate of energy transfer is \mathcal{P}_{\parallel} of Eq. (114). This is the reason why the flow of QS MHD turbulence is quasi two-dimensional (not two-dimensional) with significant U_{\parallel} .

In addition, U_{\parallel} is transported to larger wavenumbers by forward cascade. The equation for U_{\parallel} is

$$\frac{\partial U_{\parallel}}{\partial t} + \mathbf{U} \cdot \nabla U_{\parallel} = -\frac{\partial P}{\partial z} - \frac{\sigma}{\rho} \Delta^{-1} [(\mathbf{B}_0 \cdot \nabla)^2 U_{\parallel}] + \nu \nabla^2 U_{\parallel}, \quad (120)$$

which is similar to the equation of passive scalar, except the $-\partial P/\partial z$ and $(\sigma/\rho)\Delta^{-1} [(\mathbf{B}_0 \cdot \nabla)^2 U_{\parallel}]$ terms which do not appear for passive scalar. We compute flux of U_{\parallel} , Π_{\parallel} , using Eq. (118) and find this to be significant for $k > k_f$, as shown in Fig. 20.

Earlier, Favier *et al* [19] had argued that \mathbf{U}_{\perp} evolves as in 2D hydrodynamic turbulence since the Lorentz force is absent in $k_z = 0$ plane (note $\cos\theta = 0$ at $k_z = 0$ plane). Therefore, \mathbf{U}_{\perp} exhibits an inverse cascade. Favier *et al* [19] proposed that U_{\parallel} follows the following equation:

$$\frac{\partial U_{\parallel}}{\partial t} + \mathbf{U}_{\perp} \cdot \nabla_{\perp} U_{\parallel} = \nu \nabla^2 U_{\parallel}. \quad (121)$$

As described above, $-\nabla P$ of the momentum equation plays a major role in the transfer of energy from \mathbf{U}_{\perp} to U_{\parallel} . It is easy to verify that without the $-\nabla P$ term, the total energy of the parallel component, $E_{\parallel} = (1/2) \int |U_{\parallel}|^2 d\tau$, of Eq. (121) obeys

$$\frac{dE_{\parallel}}{dt} = -\nu \int U_{\parallel} \nabla^2 U_{\parallel} d\tau. \quad (122)$$

Therefore, for $\nu \neq 0$, E_{\parallel} vanishes and the flow will become two-dimensional, not quasi two-dimensional. In addition, Eqs. (12, 13) of Favier *et al* [19] refer to the modes on the $k_z = 0$ plane only. However, the other modes, specially those near $k_z = 0$ plane, are important in QS MHD turbulence. The formalism presented in the present subsection takes care of all the interactions of QS MHD in a consistent manner.

In Fig. 24 we summarise the energy transfers in QS MHD turbulence. For $k < k_f$, the perpendicular component U_{\perp} follows an inverse cascade due to the quasi two-dimensional nature of the flow, while for $k > k_f$, the parallel component U_{\parallel} cascades forward, that is from small k to large k . Both U_{\perp} and U_{\parallel} transfer energy from sectors near the equator to the ones with lower θ . The energy is primarily dissipated by Joule heating near the equator. There is an energy transfer from U_{\perp} to U_{\parallel} via pressure (not shown in the figure).

In the next section, we describe several models of QS MHD turbulence that capture the steepening of $E(k)$ quite well.

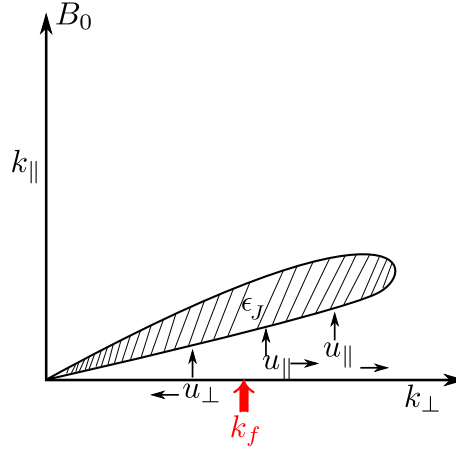


Figure 24. For large N in QS MHD turbulence, a schematic illustration of the energy transfers indicated by arrow. The strong dissipation takes place in the shaded region. \mathbf{U}_\perp exhibits an inverse cascade for $k < k_f$, while U_\parallel exhibits a forward cascade for $k > k_f$; here k_f is the forcing wavenumber. From Reddy *et al* [57]. Adopted with permission from AIP Publishing.

8. Modelling QS MHD turbulence

In Sec. 3 we described some of the earlier models of QS MHD turbulence. In this section we will review these models in the light of new findings. Before such discussions, we describe in detail the models of Verma and Reddy [74] that successfully describes the energy spectrum and flux of QS MHD turbulence for small N and very large N .

8.1. Modelling QS MHD turbulence using variable energy flux

In this subsection, we describe the turbulence model of QS MHD turbulence constructed by Verma and Reddy [74]. These models exploit the fact that the Joule dissipation depletes the energy flux and explain the energy flux and spectrum observed in numerical simulations for small N and very large N .

As discussed earlier, the QS MHD turbulence is anisotropic, hence the energy spectrum $E(\mathbf{k})$ is function of k and θ . However we make a simplification that

$$E(k, \theta) = E(k) \frac{g(\theta)}{\pi}, \quad (123)$$

where $E(k)$ is the one-dimensional energy spectrum, and $g(\theta)$ is the angular dependence of the energy spectrum. Integration of Equation (123) over θ yields

$$\int_0^\pi d\theta E(k, \theta) = E(k) \int_0^\pi \frac{g(\theta)}{\pi} d\theta = E(k). \quad (124)$$

Therefore,

$$\int_0^\pi \frac{g(\theta)}{\pi} d\theta = 1. \quad (125)$$

For the isotropic case, $g(\theta) = \text{const} = 1$.

The inertial-range energy flux $\Pi(k)$ decreases with the increase of k due to the Joule and viscous dissipation. Quantitatively, the difference between the energy fluxes $\Pi(k + dk)$ and $\Pi(k)$ is due to the energy dissipation in the shell $(k, k + dk)$, i.e.,

$$\begin{aligned}\Pi(k + dk) - \Pi(k) &= -\epsilon(k)dk \\ &= -\left\{ \int_0^\pi d\theta \left[2\nu k^2 + 2\frac{\sigma B_0^2}{\rho} \cos^2 \theta \right] E(k, \theta) \right\} dk, \quad (126)\end{aligned}$$

or

$$\frac{d\Pi(k)}{dk} = -\left[2c_1\nu k^2 + 2c_2\frac{\sigma B_0^2}{\rho} \right] E(k), \quad (127)$$

with

$$c_1 = \frac{1}{\pi} \int_0^\pi g(\theta) d\theta = 1 \quad (128)$$

$$c_2 = \frac{1}{\pi} \int_0^\pi g(\theta) \cos^2 \theta d\theta. \quad (129)$$

Based on Eq. (127) Verma and Reddy [74] constructed two models for QS MHD turbulence: model *A* for small N 's for which the energy spectrum is still a power law but steeper than Kolomogorov's $k^{-5/3}$ spectrum; and model *B* for large N 's for which the energy spectrum is exponential.

8.1.1. Model A for small interaction parameters As discussed in Sec. 5.2, for small and moderate interaction parameters, the energy spectrum is a power law but with spectral indices lower than $-5/3$ (see Table 2). Verma and Reddy [74] employed a modified form of Pope's shell spectrum [52] to model the energy spectrum for small and moderate N . In particular,

$$E(k, \theta) = E(k) \frac{g(\theta)}{\pi} = K_{Ko} [\Pi(k)]^{2/3} k^{-5/3} f_L(kL) f_\eta(k\eta) \frac{g(\theta)}{\pi}, \quad (130)$$

where K_{Ko} is the Kolmogorov constant with an approximate value of 1.5. Since N is small, the flow is nearly isotropic and $g(\theta) \approx 1$, hence $c_2 \approx 1/2$. The functions $f_L(kL)$ and $f_\eta(k\eta)$ specify the large-scale and dissipative-scale components, respectively, of the energy spectrum:

$$f_L(kL) = \left(\frac{kL}{[(kL)^2 + c_L]^{1/2}} \right)^{(5/3)+p_0}, \quad (131)$$

$$f_\eta(k\eta) = \exp \left[-\beta \left\{ [(k\eta)^4 + c_\eta^4]^{1/4} - c_\eta \right\} \right]. \quad (132)$$

Here c_L, c_η, p_0 and β are constants used by Pope [52]: $c_L \approx 6.78$, $c_\eta \approx 0.40$, $\beta \approx 5.2$, and $p_0 = 2$. Since the focus of the review is on the inertial and dissipative range, we choose $f_L(kL) = 1$.

It is important to contrast Eq. (130) with Pope's original formula. In Eq. (130), $\Pi(k)$ is k -dependent in contrast to a constant ϵ in Pope's formula. By making the flux variable, we can model the behaviour of QS MHD quite accurately. We substitute the energy spectrum of the form Eq. (130) into Eq. (127), which yields

$$\frac{d\Pi(k)}{dk} = -\left[2c_1\nu k^2 + 2c_2\frac{\sigma B_0^2}{\rho} \right] K_{Ko} (\Pi(k))^{2/3} k^{-5/3} f_\eta(k\eta). \quad (133)$$

We integrate the above equation from $k = k_1$, the starting wavenumber of the inertial range, and assume that $\Pi(k_1) = \Pi_0$. With this, the solution of Eq. (133) is

$$\begin{aligned} \left[\frac{\Pi(k)}{\Pi_0} \right]^{1/3} &= 1 - \frac{2K_{Ko}c_1}{3} \left(\frac{\nu^3}{\Pi_0\eta^4} \right)^{1/3} I_1(k\eta) - \frac{2c_2K_{Ko}\sigma B_0^2}{3\rho} \frac{\eta^{2/3}}{\Pi_0^{1/3}} I_2(k\eta) \\ &= 1 - \frac{2c_1c_3K_{Ko}}{3} I_1(k\eta) - \frac{2}{3} \frac{c_2K_{Ko}N}{\sqrt{c_3Re}} I_2(k\eta), \end{aligned} \quad (134)$$

where η is the Kolmogorov length, the dimensionless constant $c_3 = (\nu^3/\Pi_0\eta^4)^{1/3}$, and the integrals I_1 and I_2 are, respectively,

$$I_1(k\eta) = \int_{k_1\eta}^{k\eta} dk' k'^{1/3} f_\eta(k') \quad (135)$$

$$I_2(k\eta) = \int_{k_1\eta}^{k\eta} dk' k'^{-5/3} f_\eta(k'). \quad (136)$$

Verma and Reddy [74] choose $c_3 = 3.1$ in order to achieve $\Pi(k) \rightarrow 0$ for $k\eta \gg 1$ when $N = 0$ (the isotropic case). Given $\Pi(k)$ of Eq. (134), the computation of the energy spectrum is straight forward:

$$E(k) = \begin{cases} K_{Ko}\Pi_0^{2/3} k^{-5/3} f_\eta(k\eta) \left[\frac{\Pi(k)}{\Pi_0} \right]^{2/3}, & \text{if } k > k_1, \\ K_{Ko}\Pi_0^{2/3} k^{-5/3} f_L(kL) & \text{otherwise.} \end{cases} \quad (137)$$

Table 3. Table depicting various parameters used: the grid size, non-dimensional magnetic field B'_0 , the interaction parameter N calculated at the steady state, the energy spectrum, and c_2 of Eq. (129).

Grid	B'_0	N	scaling law	c_2
512 ³	0	0	$k^{-5/3}$	0.35
512 ³	0.739	0.10	$k^{-1.8}$	0.34
512 ³	1.65	0.64	$k^{-2.0}$	0.34
512 ³	2.34	1.6	$k^{-2.8}$	0.23
256 ³	25.1	130	$\exp(-0.18k)$	1.4×10^{-4}
256 ³	32.6	220	$\exp(-0.18k)$	1.3×10^{-4}

Verma and Reddy [74] then compared the aforementioned model predictions with the numerical results discussed in Sec. 5.2. The summary of their parameter values are listed in Table 3. In Figs. 25 and 26, we plot the numerically computed energy fluxes and the spectra for $N = 0, 0.10, 0.64$ and 1.6 . In the same figure we also plot the model predictions. The figures show that the model describes the numerical data quite well, and that both the energy flux and energy spectrum steepen with the increase of N . The spectral indices for various N 's are listed in Table 3. In the Table we also list c_2 for various N 's and find them to be close to $1/2$ for small N (0—1.6). Thus $g(\theta) \approx 1$, or that the flow is nearly isotropic is a good approximation till $N \approx 1.6$.

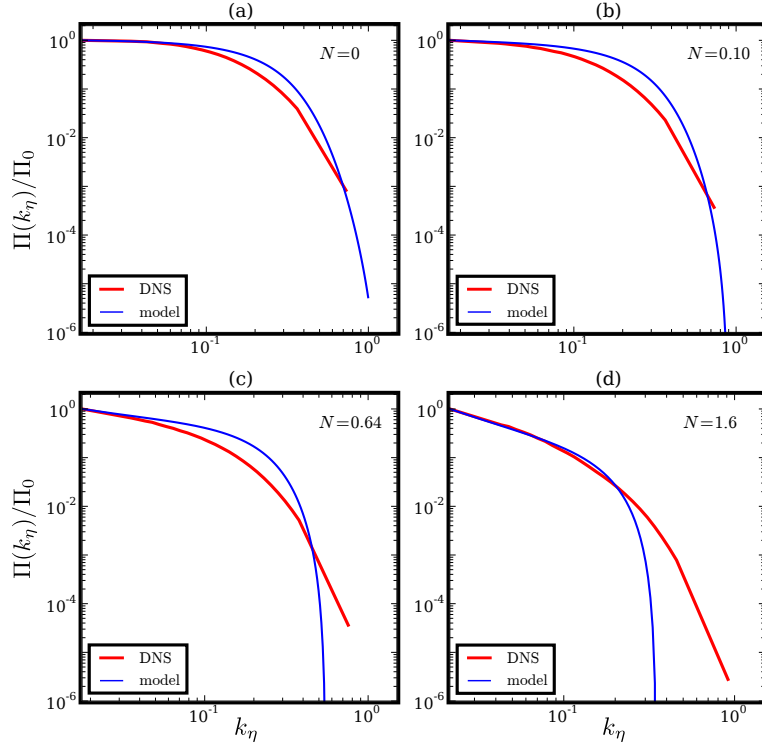


Figure 25. Plots of the normalized energy flux $\Pi(k_\eta)/\Pi_0$ for (a) $N = 0$, (b) $N = 0.10$, (c) $N = 0.64$ and (d) $N = 1.6$. The energy flux decreases with k due to Joule dissipation. From Verma and Reddy [74]. Reprinted with permission from AIP Publishing.

We remark that model *A* works well only for small N 's ($N \lesssim 1$) for which Kolmogorov's spectrum is a good starting point. This assumption breaks down for large N since the flow becomes quasi 2D. We also remark that Pao's model for fluid turbulence [51] could also be used in Eq. (130) as an alternative to the Pope's model. In the following subsection we construct another simple model that can explain the energy spectrum for very large N .

8.1.2. Model B for very large interaction parameters The Joule dissipation is strong for very large N , and it causes a rapid decrease of the energy flux with k , resulting in an exponential behaviour for the energy spectrum and energy flux (see Sec. 5.2). This behaviour is similar to the dissipative fluid flows. Therefore, for $N \gg 1$, Verma and Reddy [74] postulated that the energy spectrum follows [74]

$$E(k) = A \exp(-bk), \quad (138)$$

where A and b are constants. Using

$$\epsilon(k) = -\frac{d\Pi(k)}{dk} = (Pk^2 + Q) \exp(-bk), \quad (139)$$

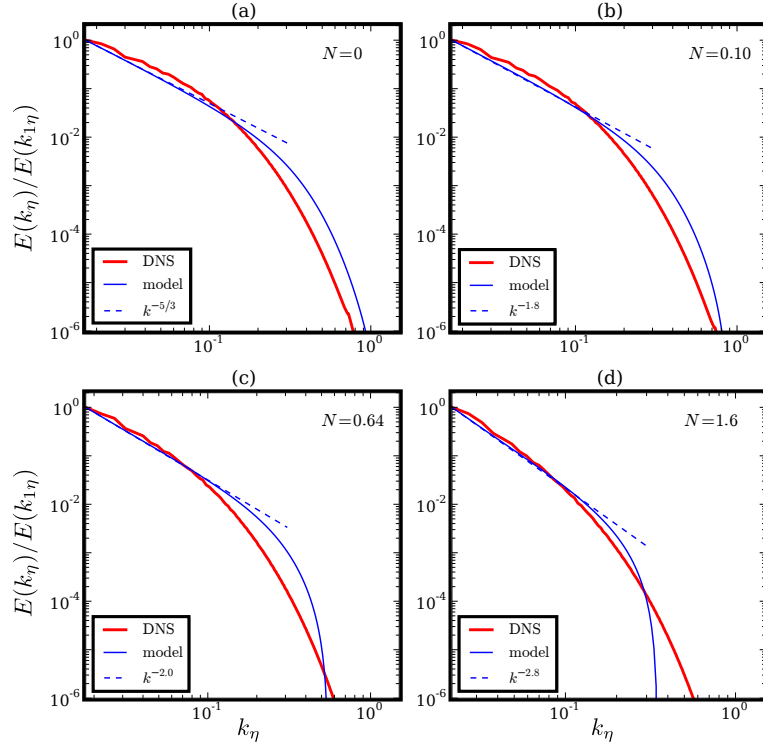


Figure 26. Plots of the normalized energy spectra $E(k\eta)$ for (a) $N = 0$, (b) $N = 0.10$, (c) $N = 0.64$ and (d) $N = 1.6$. The dashed lines are the best fit curves. Adopted with permission from Reddy [56].

where P and Q are constants, we compute $\Pi(k)$ by integration:

$$\Pi(k) = \left\{ P \left(\frac{k^2}{b} + \frac{2k}{b^2} + \frac{2}{b^3} \right) + \frac{Q}{b} \right\} \exp(-bk). \quad (140)$$

A comparison of Eq. (139) with Equation (127) yields

$$P = 2Ac_1\nu, \quad (141)$$

$$Q = 2Ac_2 \frac{\sigma B_0^2}{\rho}. \quad (142)$$

Thus, the exponential energy spectrum and flux are consistent solutions of the variable flux equation [Eq. (127)], as shown in Fig. 27.

It is important to note that the two models discussed above predict the energy spectra and fluxes for $k > k_f$ where the energy cascades in the forward direction. The regime $k < k_f$ would be affected by inverse cascade of energy, and it needs to be worked out. Unfortunately the aforementioned models A and B cannot be used for intermediate N say $N \sim 5$. A general and comprehensive model needs to be constructed for moderate N 's.

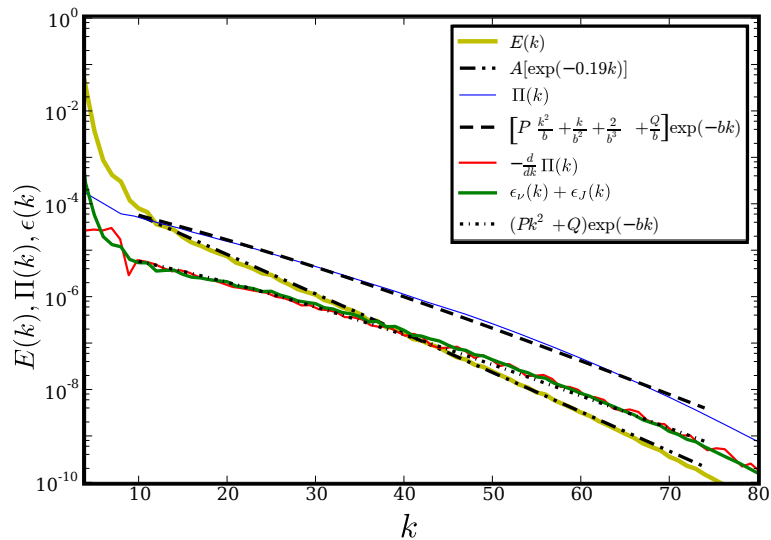


Figure 27. For $N = 220$, plot of the kinetic energy spectrum $E(k)$, flux $\Pi(k)$, total dissipation $\epsilon(k) = \epsilon_J(k) + \epsilon_\nu(k)$, and $-\frac{d}{dk}\Pi(k)$. Note that $-\frac{d}{dk}\Pi(k) \approx \epsilon(k)$. The black double dot-single dash, dashed and dash-dot lines are the best fit curves for $E(k)$, $\Pi(k)$ and $\epsilon(k)$, respectively. Adopted with permission from Reddy [56].

8.2. Review of the existing models of QS MHD turbulence

Researchers have constructed models to understand the dynamics of QS MHD turbulence. One of the critical puzzle in the field has been the steepening of the energy spectrum. It has been postulated that for large N , the QS MHD turbulence has behaviour similar to 2D hydrodynamic turbulence, hence its spectrum is expected to be close to k^{-3} rather than $k^{-5/3}$ [22, 25, 29]. Experiments [18] and numerical simulations [10, 58, 79] however reveal that the spectral index changes monotonically with N . Hence the hypothesis that $E(k) \sim k^{-3}$ is ruled out. Reddy and Verma [58], and Verma and Reddy [74] showed that the steepening of the energy spectrum is due to the decrease in energy flux with k , which occurs because of the Joule dissipation. Note that the Joule dissipation is active at all scales, unlike viscous dissipation that acts primarily at small scales. We also remark that QS MHD turbulence with very large N has exponential spectrum ($E(k) \sim \exp(-ak)$) due to extreme Joule dissipation.

Some of the early models [42, 61] of QS MHD turbulence focus on the decay laws of QS MHD. Moffatt [42] started with a linear equation for the decay of kinetic energy, and then derived a decay law for energy as $E(t) \sim t^{-1/2}$ [see Eq. (72, 75) of Sec. 3]. Present set of calculations show that the nonlinear term, possibly very weak, is active at all time. Note however that the nonlinear term dominates other terms in the $k_z = 0$ plane of the Fourier space. In Eq. (45), the term $T(k)$ yields a nonzero forward flux in the dissipation range. Thus the variable energy flux is present at all k , see for example Model *B* discussed in Sec. 8.1.2. These features invalidate Eq. (72) as a starting point for modelling the decay law for QS MHD turbulence.

In Sec. 3 we discussed how Moffatt [42] derived $E_{\parallel} = E_{\perp} = E/2$ for the asymptotic

state ($t \rightarrow \infty$). This prediction is contrary to the steady-state flow profile shown in Figs. 4 and 5 for which $E_{\perp} \gg E_{\parallel}$. The discrepancy is due to the assumptions of initial isotropic energy spectrum [Eq. (71)] and the linear decaying equation for the energy spectrum [Eq. (72)]. We believe that careful simulations and modelling are required for deriving a definitive decay law for QS MHD turbulence.

Favier *et al* [19, 20] and Reddy and Verma [58] studied the anisotropy in QS MHD turbulence by dividing the spectral space into rings. Favier *et al* [19, 20] presented the poloidal and toroidal components of the spectrum at different angles, while Reddy and Verma presented ring spectrum. Both the groups showed that QS MHD turbulence is quasi two-dimensional, however their equations for U_{\perp} and U_{\parallel} differ in a critical manner. The equation for U_{\parallel} by Favier *et al* [19], Eq. (121), does not contain $-\nabla P$ term. Reddy *et al* [57] showed that $-\nabla P$ facilitate the transfer of energy from \mathbf{U}_{\perp} to U_{\parallel} ; without $-\nabla P$ term, the total energy of the parallel component, $E_{\parallel} = (1/2) \int |U_{\parallel}|^2 d\tau$, will vanish when $\nu \neq 0$ and the flow will become two-dimensional, not quasi two-dimensional. This is a crucial factor that is expected to play a major role in other anisotropic flows, such as rotating, convective, and MHD turbulence. Refer to Sec. 7.4 for details on the energy transfers from \mathbf{U}_{\perp} to U_{\parallel} via pressure.

In summary, there is a convergence in the community that the QS MHD turbulence is quasi two-dimensional, and the energy spectrum is steeper than the hydrodynamic turbulence due to Joule dissipation. Recent turbulence models are able to explain these phenomena.

9. Bounded QS MHD flows

In this review we focus on the bulk flow of QS MHD turbulence. In the present section we provide a brief overview of QS MHD flows in bounded geometries—channel and closed box. Such flows are common in industrial applications, as well as in planetary interiors. For detailed discussion, the reader is referred to Davison [13], Moreau [46], Müller and Büher [47], and Zikanov *et al* [78].

Bounded flows have boundary layers near the walls. The boundary layer of QS MHD is called *Hartmann layer*. The bounded flow of QS MHD differs from hydrodynamic flows in several aspects. The Ampère force ($\mathbf{J} \times \mathbf{B}$) in the bulk produces additional drag force in QS MHD. Also, the conducting walls support electric current, which is not the case for hydrodynamic flows; such currents tend to accelerate the flow near the wall leading to jets. In the following discussion, we only touch upon some of these features.

9.1. QS MHD over a plate and in a channel: linear limit

First, we study the flow over a flat plate as shown in Fig. 28(a). We assume that $\mathbf{u} = u_0 \hat{x}$ as $z \rightarrow \infty$, and $\mathbf{u} = 0$ (no-slip boundary condition) at $z = 0$. We also assume presence of an external magnetic field $\mathbf{B} = B_0 \hat{z}$, absence of an external electric field, and that the fluid is forced by a constant pressure gradient $-\partial p / \partial x$. Hence the electric current

density is

$$\mathbf{J} = \sigma \mathbf{u} \times \mathbf{B}_0 = -\sigma u B_0 \hat{y}, \quad (143)$$

where σ is the electric conductivity of the fluid. Therefore the force density is

$$\mathbf{f}_L = \mathbf{J} \times \mathbf{B}_0 = -\sigma u B_0^2 \hat{x}. \quad (144)$$

For simplicity, we assume that the nonlinear term is negligible. Under steady state, the force balance yields

$$\rho \nu \frac{\partial^2 u}{\partial z^2} - \sigma B_0^2 u = \frac{\partial p}{\partial x}, \quad (145)$$

where ρ, ν are respectively the density and kinematic viscosity of the fluid. For a constant $\partial p / \partial x$, the above equation has the following particular solution

$$u_{\text{particular}} = u_0 = \frac{1}{\sigma B_0^2} \left(-\frac{\partial p}{\partial x} \right), \quad (146)$$

and the following homogeneous solution

$$u_{\text{homog}} = A \exp(-z/\delta) + C \exp(z/\delta), \quad (147)$$

where A, B are constants, and $\delta = [\rho \nu / (\sigma B_0^2)]^{1/2}$. The solution $u = u_{\text{homog}} + u_{\text{particular}}$ with boundary condition $u = 0$ at $z = 0$, and finite u as $z \rightarrow \infty$ yields $C = 0$. Hence the solution is

$$u = u_0 [1 - \exp(-z/\delta)]. \quad (148)$$

It is easy to note that the Lorentz force induces additional suppression in the flow.

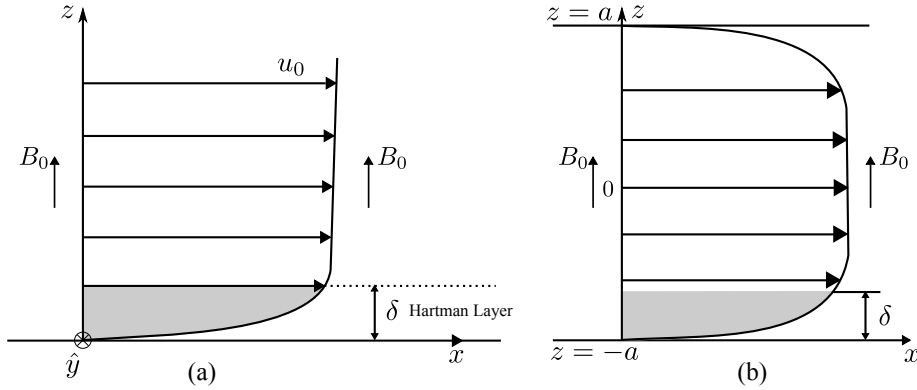


Figure 28. (a) QS MHD flow over a flat plate. (b) QS MHD flow in a channel.

In Fig. 28, the region from $z = 0$ to $z = \delta$ where the velocity increase exponentially from 0 to $\approx u_0$ is called the *Hartmann layer*, and the quantity δ is the *width of the Hartmann layer*. The Hartmann number is defined as the square root of the ratio of the Lorentz force and the viscous force:

$$\text{Ha} = \sqrt{\frac{\sigma B_0^2 u / \rho}{\nu u / a^2}} = B_0 a \sqrt{\frac{\sigma}{\rho \nu}}. \quad (149)$$

Clearly

$$\frac{a}{\delta} = \text{Ha}. \quad (150)$$

Note that

$$N \times \text{Re} = \text{Ha}^2. \quad (151)$$

Using Eq. (150) we deduce that

$$\delta = \frac{a}{\sqrt{\text{Re}}} \frac{1}{\sqrt{N}} \approx \frac{\delta_\nu}{\sqrt{N}}, \quad (152)$$

where δ_ν is the thickness of the viscous boundary layer. Thus, the Hartmann layer is thinner than the viscous boundary layer by a factor of \sqrt{N} .

A related problem is the flow in a channel shown in Fig. 28(b). The walls are located at $z = \pm a$ at which we employ no-slip boundary condition ($\mathbf{u} = 0$). The equation of the flow under the linear approximation is same as Eq. (145), whose homogeneous solution is

$$u_{\text{homog}} = A \cosh(z/\delta), \quad (153)$$

and the particular solution is same as that of Eq. (146). The odd solution $\sinh(z/\delta)$ is absent due to the even symmetry about $z = 0$. Therefore, for the no-slip condition at $z = \pm a$, the solution for the velocity is $\mathbf{u} = u\hat{x}$ with

$$u = u_0 \left[1 - \frac{\cosh(z/\delta)}{\cosh(a/\delta)} \right]. \quad (154)$$

The above solution yields $u = u_0[1 - 1/\cosh(a/\delta)] \approx u_0$ at $z = 0$.

The above equations are linear hence they could be solved analytically. The full QS MHD equations with nonlinearity are more difficult, and they are typically solved using numerical simulations. We describe these issues briefly in the next subsection.

9.2. QS MHD turbulence in a channel

For large Re and N , Eq. (152) shows that the Hartmann layer is very thin, whose resolution in numerical simulations is one of the most difficult issues of QS MHD turbulence research. Boeck *et al* [5] and Krasnov *et al* [35] performed spectral simulations using Fourier basis for the periodic direction, and Chebyshev polynomials for the wall direction(s). Boeck *et al* [5] simulated low- Rm MHD flows in a channel with no-slip boundary conditions for $\text{Re} = 8000$ and $\text{Ha} = 80$ and observed recurring transitions between two-dimensional and three-dimensional states in the flow. Dymkou and Poth erat [17] and Kornet and Poth erat [32] invented a new spectral scheme based on basis functions suitable for QS channel flow; their method is quite efficient since their basis functions contain the Hartmann layer. Finite difference, finite volume, and finite element methods are also used to solve flows with walls [70]. Some of these methods are discussed in Sec. 5.

A natural question is the role of nonlinearity in QS MHD turbulence. The QS MHD flows above a flat plate and in a channel discussed in Sec. 9.2 are quite stable,

primarily due to the fact that the Couette and channel flows are quite stable [16]. In Sec. 4 we described how perturbed (e.g., grid-generated turbulence in experiments) QS MHD turbulence exhibit powerlaw and exponential energy spectra. However, it will be interesting to compare the properties of turbulence in the bulk part of a channel (e.g, as in Boeck *et al* [5]) with the spectral results discussed in the present paper.

A Generic feature of the aforementioned flows is that the Lorentz force provides additional drag (in addition to the viscous drag), and hence the flow is slower than its hydrodynamic counterpart. This is due to the induced electric currents in the flow. Additional side walls create further complexity due to the wall currents; for such flows, the induced electric currents accelerate the flow near the wall leading to strong near-wall jets. For details, refer to Moreau [46] and Müller and Bühler [47].

9.3. QS MHD in a box

Sommeria [63], Herault *et al* [21], Klein and Proth erat [26], and Proth erat and Klein [54] performed experiments on liquid metals in a closed box (see Fig. 1), and analysed the flow in great detail. They reported quasi two-dimensionalization of the flow for strong B_0 . Klein and Poth erat [26] and Poth erat and Klein [54] also discussed how the flow becomes three-dimensional due to inertia and induced currents. In this review we do not cover these topics in detail, and only discuss some of the patterns observed in two-dimensional QS MHD flows.

Sommeria [63] and Sommeria and Moreau [64] studied a forced liquid-metal flow in which magnets with alternating polarities located at the bottom of the box drive the flow. They employed the following equation of motion for the flow:

$$\frac{\partial \mathbf{u}_\perp}{\partial t} + (\mathbf{u}_\perp \cdot \nabla) \mathbf{u}_\perp = -\nabla_\perp(p/\rho) - \frac{\mathbf{u}_\perp}{\tau_H} + \nu \nabla^2 \mathbf{u}_\perp, \quad (155)$$

where Hartmann damping time $\tau_H = \delta/u_{\text{small}} = (a/B_0)(\rho a/\sigma\nu)^{1/2}$ with $u_{\text{small}} = \nu/a$. The Lorentz force in Eq. (155) is suppressed by a factor $\delta/a = \text{Ha}^{-1}$ compared to that in a periodic box [see Eq. (40)]. A nondimensional version of the above equation is

$$\frac{\partial \mathbf{U}_\perp}{\partial t} + (\mathbf{U}_\perp \cdot \nabla) \mathbf{U}_\perp = -\nabla_\perp P - \frac{\mathbf{U}_\perp}{\text{Rh}} + \frac{1}{\text{Re}} \nabla^2 \mathbf{U}_\perp, \quad (156)$$

where $\text{Re} = U_0 L/\nu$, $\text{Rh} = \tau_H L/U_0$, and \mathbf{U}_\perp, P are nondimensional variables.

Sommeria [63] and Herault *et al* [21] performed experiments on mercury contained in box of size 12cm \times 12cm \times 2cm. The fluid was forced using 36 electromagnets of alternating magnetic polarities. For a set of parameters, Sommeria observed $k^{-5/3}$ energy spectrum corresponding to two-dimensional hydrodynamic turbulence (the inverse cascade regime as predicted by Kraichnan [34]); he also reported large-scale structures for another set of parameters.

Mishra *et al* [41] simulated the setup of Sommeria [63] and Herault *et al* [21] for a set of Re and Rh . For a given Re , with the increase of Rh , Mishra *et al* observed the following set of bifurcations: stable 6×6 vortex structures, temporal and spatial chaos, flow reversals, and large-scale circulation at the box size (the condensate state). Note

that large Rh corresponds lower B_0 or lower Lorentz force. Thus, Mishra *et al* [41] show that large B_0 yields same patterns as the forcing configuration (6×6 vortex structures), but lower B_0 leads to inverse cascade of energy and consequent coalescence of flow structures, similar to those observed in 2D hydrodynamic turbulence.

Here we close our discussion on QS MHD in a bounded box. In the next section we summarise the present status of the field.

10. Conclusions

In this review we describe the main results of QS MHD turbulence obtained using experimental, numerical, and modelling. A summary of the results presented in the review is as follows:

- (i) The imposed external magnetic field creates flow anisotropy that increases with the increase of the external magnetic field B_0 or the interaction parameter (N). For moderate and large N , the QS MHD flow is quasi two-dimensional with strong U_\perp and weak U_\parallel , where U_\perp and U_\parallel are the perpendicular and parallel components of the velocity field relative to the mean magnetic field \mathbf{B}_0 . The energy spectrum $E(k)$ is steeper than Kolmogorov's spectrum ($k^{-5/3}$) with the spectral index decreasing with the increase of N . For very large N , $E(k) \sim \exp(-bk)$, where b is a constant. The results from numerical simulations, experiments, and model of Sec. 8 are in good agreement with each other.
- (ii) In QS MHD turbulence, the energy flux $\Pi(k)$ decreases with k due to the Joule dissipation. The steepening of the energy spectrum in comparison to Kolmogorov's spectrum is due to this variable energy flux.
- (iii) For large N , the energy is concentrated near the equatorial region (near $k_z = 0$ plane). In this regime, U_\perp dominates at small k , while U_\parallel dominates at large k . The pressure facilitates energy transfer from U_\perp to U_\parallel .
- (iv) The anisotropy in QS MHD turbulence is quantified using the ring spectrum and ring-to-ring energy transfers. Studies reveal that energy flows from $\theta \approx \pi/2$ (near the equatorial plane) to lower θ . Also, the energy flux of the perpendicular component, Π_\perp , is negative at small k ($k < k_f$ where k_f is the forcing wavenumber) indicating an inverse cascade of U_\perp . However the energy flux of parallel component, Π_\parallel , is positive for $k > k_f$, thus U_\parallel exhibits forward cascade.

In this review we focus on the turbulence phenomenology of the bulk flow in QS MHD turbulence. There are however many experiments [40] and numerical simulations [5] that focus on the flow in a channel that includes a Hartman layer; researchers have not studied the spectrum and flux of such flows in detail. It will be interesting to compare $E(k)$ in a channel with the theoretical results presented in this review. For example, it is reasonable to conjecture that in a channel flow involving QS MHD, $E(k)$ could be exponential as reported in Sections 5 and 8. Such studies may prove very

useful for modelling channel flows, specially for the liquid metal blanket of the ITER (International Thermonuclear Experimental Reactor) project.

The model of Sec. 8 needs further refinements. For example, the assumption that $E(k, \theta) = E(k)g(\theta)$ needs to be validated against numerical results. In addition, the model needs to be extended to intermediate N (for example, $1 < N < 100$) where we observe steep power-law and quasi 2D behaviour. For such flows, we need to start with $E(k) \sim k^{-3}$ that corresponds to constant enstrophy flux. Also, the model of Sec. 8 would be useful for large-eddy simulations of QS MHD turbulence, as well as for constructing turbulence models for realistic QS MHD flows.

Most flows in nature are anisotropic due to (a) external applied field, e.g. buoyancy, external magnetic field, or (b) inhomogeneous boundary conditions, e.g. in a channel with no-slip boundary conditions at the top and bottom plates. Researchers have developed tools to study anisotropy, for example, see Sagaut and Cambon [60], Davidson [14], Shabalín [62] and references therein. They have proposed poloidal and toroidal decomposition, ring decomposition similar to ours, mean angle θ_Q of Eq. (94), etc. The tools described in this review complement the tools proposed by these authors, and they would be useful for studying anisotropy in generic turbulent systems. We also remark that such quantification of turbulence will help us model the diffusion of particles in turbulent MHD turbulence as well [37, 49].

It is interesting to compare the anisotropy in QS MHD with other related systems. MHD turbulence with strong external magnetic field, and strongly rotating turbulence tend to exhibit quasi 2D behaviour [13, 14, 50, 68, 60] with $U_{\perp} \gg U_{\parallel}$. This feature is similar to that of QS MHD turbulence. In Rayleigh-Bénard flow however $U_{\perp} < U_{\parallel}$, but U_{\perp} and U_{\parallel} are comparable, hence the flow is nearly isotropic [48]. The above conclusions have been drawn using the tools discussed in this review.

The external fields like magnetic field (in MHD and QS MHD) or buoyancy, as well as rotation, makes the flow anisotropic. It has been observed that the external magnetic field and rotation makes the flow quasi 2D [13, 14, 50, 60, 67, 68] with $U_{\perp} \gg U_{\parallel}$, that is, the flow perpendicular to the anisotropic axis is stronger than its parallel counterpart. However in Rayleigh-Bénard convection, the behaviour is quite different. The thermal plumes accelerate the flow along the buoyancy direction, which yields $U_{\parallel} > U_{\perp}$. However, recently Nath *et al* [48] and Verma *et al* [75] showed that U_{\parallel} and U_{\perp} are comparable, hence the flow is much less anisotropic than QS MHD turbulence for large interaction parameters. Thus the nature of anisotropy is different in these systems. Yet, the tools discussed in this paper have been applied to study diverse anisotropic systems [13, 14, 48, 50, 60, 67, 68, 75].

Turbulence remains an unsolved phenomena. We hope that the tools described in this review will provide further insights into this phenomena, specially those related to anisotropy.

Acknowledgement

Some of the material of the review is based on the thesis work of Sandeep Reddy, and collaborative work with Raghendra Kumar. I am grateful to both of them for the fruitful collaboration and exciting discussions. I thank the colleagues of our laboratory at IIT Kanpur specially Anando Chatterjee and Abhishek Kumar for ideas and help. I am grateful to colleagues of ULB Brussels—Daniele Carati, Bernard Knaepen, Xavier Albets, Paolo Burattini, and Maxime Kinet—for valuable ideas and suggestions when I was new to this field. I also benefitted from the conversations with Thomas Boeck, Jörg Schumacher, Andre Thess, Stephan Fauve, and V. Eswaran, and from the useful comments of the anonymous referees. I thank Roshan Bhaskaran for help in making the figures.

Some results of the review are based on simulations performed on the HPC system and Chaos cluster of IIT Kanpur, India. This work was supported by a research grants 2009/36/81-BRNS from Board of Research in Nuclear Science, Department of Atomic Energy, Government of India, and Indo-Russian project (DST-RSF) project INT/RUS/RSF/P-03 from Department of Science and Technology, India.

Appendix A. Energy transfers in anisotropic turbulence

The turbulence in QS MHD turbulence is anisotropic due to the external magnetic field. In this appendix we quantify the energy transfers between the perpendicular and parallel components of the velocity field. To derive the formulae for the energy transfers, we focus on a wavenumber triad $(\mathbf{k}', \mathbf{p}, \mathbf{q})$ that satisfies $\mathbf{k}' + \mathbf{p} + \mathbf{q} = 0$. For convenience we denote $\mathbf{k}' = -\mathbf{k}$.

Following Dar *et al* [12] and Verma [71], we derive the following equations from Eqs. (40) and (41):

$$\frac{\partial E_{\perp}(\mathbf{k}')}{\partial t} = S_{\perp}(\mathbf{k}'|\mathbf{p}|\mathbf{q}) + S_{\perp}(\mathbf{k}'|\mathbf{q}|\mathbf{p}) + \mathcal{P}_{\perp}(\mathbf{k}') - D_{\perp}(\mathbf{k}'), \quad (\text{A.1})$$

$$\frac{\partial E_{\parallel}(\mathbf{k}')}{\partial t} = S_{\parallel}(\mathbf{k}'|\mathbf{p}|\mathbf{q}) + S_{\parallel}(\mathbf{k}'|\mathbf{q}|\mathbf{p}) + \mathcal{P}_{\parallel}(\mathbf{k}') - D_{\parallel}(\mathbf{k}'), \quad (\text{A.2})$$

where $E_{\perp}(\mathbf{k}) = E_{\perp}(\mathbf{k}') = \frac{1}{2}|\hat{\mathbf{U}}_{\perp}(\mathbf{k})|^2$ and $E_{\parallel}(\mathbf{k}) = E_{\parallel}(\mathbf{k}') = \frac{1}{2}|\hat{\mathbf{U}}_{\parallel}(\mathbf{k})|^2$ are respectively the energies of the perpendicular and parallel components of the velocity field, and

$$S_{\perp}(\mathbf{k}'|\mathbf{p}|\mathbf{q}) = -\Im\{[\mathbf{k}' \cdot \hat{\mathbf{U}}(\mathbf{q})][\hat{\mathbf{U}}_{\perp}(\mathbf{k}') \cdot \hat{\mathbf{U}}_{\perp}(\mathbf{p})]\}, \quad (\text{A.3})$$

$$S_{\parallel}(\mathbf{k}'|\mathbf{p}|\mathbf{q}) = -\Im\{[\mathbf{k}' \cdot \hat{\mathbf{U}}(\mathbf{q})][\hat{\mathbf{U}}_{\parallel}(\mathbf{k}')\hat{\mathbf{U}}_{\parallel}(\mathbf{p})]\}, \quad (\text{A.4})$$

$$\mathcal{P}_{\perp}(\mathbf{k}') = \Im\{[\mathbf{k} \cdot \hat{\mathbf{U}}_{\perp}^*(\mathbf{k})]\hat{P}(\mathbf{k})\}, \quad (\text{A.5})$$

$$\mathcal{P}_{\parallel}(\mathbf{k}') = \Im\{[k_{\parallel}\hat{\mathbf{U}}_{\parallel}^*(\mathbf{k})]\hat{P}(\mathbf{k})\}, \quad (\text{A.6})$$

where $\Re, \Im, *$ represent the real part, imaginary part, and complex conjugate of a complex number respectively. The terms $D_{\perp}(\mathbf{k}')$ and $D_{\parallel}(\mathbf{k}')$ are the total dissipation rates (viscous + Joule) of $E_{\perp}(\mathbf{k}')$ and $E_{\parallel}(\mathbf{k}')$ respectively. Equations (A.1) and (A.2) indicate that the mode \mathbf{k}' receives energy from the modes \mathbf{p} and \mathbf{q} . Similarly, we can also derive

$$\frac{\partial E_{\perp}(\mathbf{p})}{\partial t} = S_{\perp}(\mathbf{p}|\mathbf{q}|\mathbf{k}') + S_{\perp}(\mathbf{p}|\mathbf{k}'|\mathbf{q}) + \mathcal{P}_{\perp}(\mathbf{p}) - D_{\perp}(\mathbf{p}), \quad (\text{A.7})$$

$$\frac{\partial E_{\parallel}(\mathbf{p})}{\partial t} = S_{\parallel}(\mathbf{p}|\mathbf{q}|\mathbf{k}') + S_{\parallel}(\mathbf{p}|\mathbf{k}'|\mathbf{q}) + \mathcal{P}_{\parallel}(\mathbf{p}) - D_{\parallel}(\mathbf{p}), \quad (\text{A.8})$$

$$\frac{\partial E_{\perp}(\mathbf{q})}{\partial t} = S_{\perp}(\mathbf{q}|\mathbf{k}'|\mathbf{p}) + S_{\perp}(\mathbf{q}|\mathbf{p}|\mathbf{k}') + \mathcal{P}_{\perp}(\mathbf{q}) - D_{\perp}(\mathbf{q}), \quad (\text{A.9})$$

$$\frac{\partial E_{\parallel}(\mathbf{q})}{\partial t} = S_{\parallel}(\mathbf{q}|\mathbf{k}'|\mathbf{p}) + S_{\parallel}(\mathbf{q}|\mathbf{p}|\mathbf{k}') + \mathcal{P}_{\parallel}(\mathbf{q}) - D_{\parallel}(\mathbf{q}). \quad (\text{A.10})$$

Using $\mathbf{k} \cdot \hat{\mathbf{U}}(\mathbf{k}) = 0$, we can show that

$$\mathcal{P}_{\perp}(\mathbf{k}') + \mathcal{P}_{\parallel}(\mathbf{k}') = 0, \quad (\text{A.11})$$

$$S_{\perp}(\mathbf{k}'|\mathbf{p}|\mathbf{q}) = -S_{\perp}(\mathbf{p}|\mathbf{k}'|\mathbf{q}), \quad (\text{A.12})$$

$$S_{\parallel}(\mathbf{k}'|\mathbf{p}|\mathbf{q}) = -S_{\parallel}(\mathbf{p}|\mathbf{k}'|\mathbf{q}). \quad (\text{A.13})$$

and

$$\begin{aligned} & S_{\perp}(\mathbf{k}'|\mathbf{p}|\mathbf{q}) + S_{\perp}(\mathbf{k}'|\mathbf{q}|\mathbf{p}) + S_{\perp}(\mathbf{p}|\mathbf{k}'|\mathbf{q}) \\ & + S_{\perp}(\mathbf{p}|\mathbf{q}|\mathbf{k}') + S_{\perp}(\mathbf{q}|\mathbf{k}'|\mathbf{p}) + S_{\perp}(\mathbf{q}|\mathbf{p}|\mathbf{k}') = 0, \end{aligned} \quad (\text{A.14})$$

$$\begin{aligned}
& S_{\parallel}(\mathbf{k}'|\mathbf{p}|\mathbf{q}) + S_{\parallel}(\mathbf{k}'|\mathbf{q}|\mathbf{p}) + S_{\parallel}(\mathbf{p}|\mathbf{k}'|\mathbf{q}) \\
& + S_{\parallel}(\mathbf{p}|\mathbf{q}|\mathbf{k}') + S_{\parallel}(\mathbf{q}|\mathbf{k}'|\mathbf{p}) + S_{\parallel}(\mathbf{q}|\mathbf{p}|\mathbf{k}') = 0.
\end{aligned} \tag{A.15}$$

Using the above equations and ignoring the dissipation terms, we conclude that

$$\frac{\partial}{\partial t} [E_{\perp}(\mathbf{k}') + E_{\perp}(\mathbf{p}) + E_{\perp}(\mathbf{q})] = \mathcal{P}_{\perp}(\mathbf{k}') + \mathcal{P}_{\perp}(\mathbf{p}) + \mathcal{P}_{\perp}(\mathbf{q}), \tag{A.16}$$

$$\frac{\partial}{\partial t} [E_{\parallel}(\mathbf{k}') + E_{\parallel}(\mathbf{p}) + E_{\parallel}(\mathbf{q})] = -[\mathcal{P}_{\perp}(\mathbf{k}') + \mathcal{P}_{\perp}(\mathbf{p}) + \mathcal{P}_{\perp}(\mathbf{q})]. \tag{A.17}$$

Therefore, we can make the following conclusions regarding the energy transfers for the parallel and perpendicular components of the velocity field:

- (i) The sum of Equations (A.16) and (A.17) shows that the total energy (sum of the perpendicular and parallel components) for a triad is conserved. However, there is an energy transfer between the perpendicular and parallel components via pressure.
- (ii) The perpendicular component $\hat{\mathbf{U}}_{\perp}(\mathbf{k}')$ receives energy by an amount $S_{\perp}(\mathbf{k}'|\mathbf{p}|\mathbf{q})$ from $\hat{\mathbf{U}}_{\perp}(\mathbf{p})$ with $\hat{\mathbf{U}}(\mathbf{q})$ as a mediator. Symmetrically, it also receives energy by an amount $S_{\perp}(\mathbf{k}'|\mathbf{q}|\mathbf{p})$ from $\hat{\mathbf{U}}_{\perp}(\mathbf{q})$ via $\hat{\mathbf{U}}(\mathbf{p})$. The parallel component $\hat{U}_{\parallel}(\mathbf{k}')$ receives energy by amounts $S_{\parallel}(\mathbf{k}'|\mathbf{p}|\mathbf{q})$ and $S_{\parallel}(\mathbf{k}'|\mathbf{q}|\mathbf{p})$ respectively from the modes $\hat{U}_{\parallel}(\mathbf{p})$ and $\hat{U}_{\parallel}(\mathbf{q})$ with $\hat{\mathbf{U}}(\mathbf{q})$ and $\hat{\mathbf{U}}(\mathbf{p})$ acting as the respective mediators.
- (iii) Equation (A.1) implies that the perpendicular component $\hat{\mathbf{U}}_{\perp}(\mathbf{k}')$ gains energy from the $\mathcal{P}_{\perp}(\mathbf{k}')$ term, which arises due to the pressure. Since $\mathcal{P}_{\perp}(\mathbf{k}') = -\mathcal{P}_{\parallel}(\mathbf{k}')$, the energy gained by $\hat{\mathbf{U}}_{\perp}(\mathbf{k}')$ via pressure is the same as the energy lost by $\hat{U}_{\parallel}(\mathbf{k}')$ [see Equation (A.2)]. Hence, the energy transfer between the parallel and perpendicular components occur via pressure.
- (iv) Since $\mathbf{k}' = -\mathbf{k}$, $E(\mathbf{k}') = E(\mathbf{k})$. It is customary to express the energy transfers in terms of $(\mathbf{k}, \mathbf{p}, \mathbf{q})$. For the same we replace $\hat{\mathbf{U}}(\mathbf{k}') = \hat{\mathbf{U}}^*(\mathbf{k})$.

We use the aforementioned formulas to compute the energy fluxes of the perpendicular and parallel components of the velocity field. The energy flux $\Pi_{\perp}(k_0)$ for the perpendicular component of the velocity field for a wavenumber sphere of radius k_0 is defined as the net energy transferred from the modes $\mathbf{U}_{\perp}(\mathbf{p})$ residing inside the sphere to the modes $\mathbf{U}_{\perp}(\mathbf{k})$ outside the sphere, i.e.,

$$\Pi_{\perp}(k_0) = \sum_{|\mathbf{k}| \geq k_0} \sum_{|\mathbf{p}| < k_0} S_{\perp}(\mathbf{k}|\mathbf{p}|\mathbf{q}). \tag{A.18}$$

A similar formula for $\Pi_{\parallel}(k_0)$, the flux of the parallel velocity component, is

$$\Pi_{\parallel}(k_0) = \sum_{|\mathbf{k}| \geq k_0} \sum_{|\mathbf{p}| < k_0} S_{\parallel}(\mathbf{k}|\mathbf{p}|\mathbf{q}). \tag{A.19}$$

The total flux is the sum of the above two fluxes.

References

- [1] A. Alemany, R. Moreau, P. L. Sulem, and U. Frisch. Influence of an external magnetic field on homogeneous MHD turbulence. *J de Mecanique*, 18:277, 1979.
- [2] V. Bandaru, T. Boeck, D. Krasnov, and J. Schumacher. A hybrid finite difference-boundary element procedure for the simulation of turbulent MHD duct flow at finite magnetic Reynolds number. *J. Comp. Phys.*, 304:320–339, 2016.
- [3] L. Biferale and I. Procaccia. Anisotropy in turbulent flows and in turbulent transport. *Phys. Rep.*, 414(2-3):43–164, 2005.
- [4] D. Biskamp. *Nonlinear Magnetohydrodynamics*. Cambridge University Press, Cambridge, 1993.
- [5] T. Boeck, D. Krasnov, D. Krasnov, A. Thess, and O. Zikanov. Large-scale intermittency of liquid-metal channel flow in a magnetic field. *Phys. Rev. Lett.*, 101:244501, 2008.
- [6] G. Boffetta and R. E. Ecke. Two-Dimensional Turbulence. *Annu. Rev. Fluid Mech.*, 44:427–451, 2012.
- [7] S. I. Braginskii. Transport Processes in a Plasma. *Reviews of Plasma Physics*, 1:205–311, 1965.
- [8] H. Branover, A. Eidelman, M. Nagarny, and M. Kireev. Magnetohydrodynamic simulation of quasi-two-dimensional geophysical turbulence. In H. Branover and Y. Unger, editors, *Progress in Turbulence Research*, page 64. 1994.
- [9] P. Burattini, M. Kinet, D. Carati, and B. Knaepen. Anisotropy of velocity spectra in quasistatic magnetohydrodynamic turbulence. *Phys. Fluids*, 20(6):065110, 2008.
- [10] P. Burattini, M. Kinet, D. Carati, and B. Knaepen. Spectral energetics of quasi-static MHD turbulence. *Physica D*, 237(1):2062–2066, 2008.
- [11] P. Burattini, O. Zikanov, and B. Knaepen. Decay of magnetohydrodynamic turbulence at low magnetic Reynolds number. *J. Fluid Mech.*, 657:502–538, 2010.
- [12] G. Dar, M. K. Verma, and V. Eswaran. Energy transfer in two-dimensional magnetohydrodynamic turbulence: formalism and numerical results. *Physica D*, 157(3):207–225, 2001.
- [13] P. A. Davidson. *An Introduction to Magnetohydrodynamics*. Cambridge University Press, Cambridge, 2001.
- [14] P. A. Davidson. *Turbulence in Rotating, Stratified and Electrically Conducting Fluids*. Cambridge University Press, Cambridge, 2013.
- [15] P. A. Davidson. *Turbulence*. Oxford University Press, Oxford, 2nd edition, 2015.
- [16] P. G. Drazin and W. H. Reid. *Hydrodynamic Stability*. Cambridge University Press, 2004.
- [17] V. Dymkou and A. Pothérat. Spectral methods based on the least dissipative modes for wall bounded MHD flows. *Theor. Comput. Fluid Dyn.*, 23(6):535–555, 2009.
- [18] S. Eckert, G. Gerbeth, and W. Witke. MHD turbulence measurements in a sodium channel flow exposed to a transverse magnetic field. *Int. J. Heat Mass Transfer*, 22(3):358–364, 2001.
- [19] B. Favier, F. S. Godeferd, C. Cambon, and A. Delache. On the two-dimensionalization of quasistatic magnetohydrodynamic turbulence. *Phys. Fluids*, 22(7):075104, 2010.
- [20] B. F. N. Favier, F. S. Godeferd, C. Cambon, A. Delache, and W. J. T. Bos. Quasi-static magnetohydrodynamic turbulence at high Reynolds number. *J. Fluid Mech.*, 681:434–461, 2011.
- [21] J. Hérault, F. Pétrélis, and S. Fauve. Experimental observation of $1/f$ noise in quasi-bidimensional turbulent flows. *EPL*, 111(4):44002, 2015.
- [22] M. Hossain. Inverse energy cascades in three-dimensional turbulence. *Phys. Fluids B*, 3(3):511–514, 1991.
- [23] T. Ishida and Y. Kaneda. Small-scale anisotropy in magnetohydrodynamic turbulence under a strong uniform magnetic field. *Phys. Fluids*, 19(7):075104, 2007.
- [24] T. Ishihara, K. Yoshida, and Y. Kaneda. Anisotropic Velocity Correlation Spectrum at Small Scales in a Homogeneous Turbulent Shear Flow, *Phys. Rev. Lett.*, 15:154501, 2002.
- [25] L. G. Kit and A. B. Tsinober. Possibility of generating and investigating two-dimensional turbulence in a strong magnetic field (Two dimensional MHD turbulent flow generation in strong magnetic field). *Magnitnaia Gidrodinamika*, 7:27–34, 1971.

- [26] R. Klein and A. Poth erat. Appearance of Three Dimensionality in Wall-Bounded MHD Flows. *Phys. Rev. Lett.*, 104(3):034502, 2010.
- [27] B. Knaepen, S. C. Kassinos, and D. Carati. Magnetohydrodynamic turbulence at moderate magnetic Reynolds number. *J. Fluid Mech.*, 513:199–220, 1999.
- [28] B. Knaepen and R. Moreau. Magnetohydrodynamic turbulence at low magnetic Reynolds number. *Annu. Rev. Fluid Mech.*, 40:25–45, 2008.
- [29] Y. B. Kolesnikov and A. B. Tsinober. Experimental investigation of two-dimensional turbulence behind a grid. *Fluid Dyn.*, 9(4):621–624, 1976.
- [30] A. N. Kolmogorov. Dissipation of Energy in Locally Isotropic Turbulence. *Dokl Acad Nauk SSSR*, 32(1):16–18, 1941.
- [31] A. N. Kolmogorov. The local structure of turbulence in incompressible viscous fluid for very large Reynolds numbers. *Dokl Acad Nauk SSSR*, 30(4):301–305, 1941.
- [32] K. Kornet and A. Poth erat. A method for spectral DNS of low R_m channel flows based on the least dissipative modes. *J. Comput. Phys.*, 298:266–279, 2015.
- [33] R. H. Kraichnan. The structure of isotropic turbulence at very high Reynolds numbers. *J. Fluid Mech.*, 5:497–543, 1959.
- [34] R. H. Kraichnan. Inertial ranges in two-dimensional turbulence. *Phys. Fluids*, 10:1417, 1967.
- [35] D. Krasnov, O. Zikanov, J. Schumacher, and T. Boeck. Magnetohydrodynamic turbulence in a channel with spanwise magnetic field. *Phys. Fluids*, 20(9):095105, 2008.
- [36] S. Kurien and K. R. Sreenivasan. Anisotropic scaling contributions to high-order structure functions in high-Reynolds-number turbulence. *Phys. Rev. E*, 62(2):2206–2212, 2000.
- [37] C. C. Lalescu, I. Petrisor, M. Negrea, and B. Teaca. Test particles transport in two-dimensional turbulent plasma. *Physics AUC*, 24:97–103, 2014.
- [38] M. Lesieur. *Turbulence in Fluids*. Springer Science & Business Media, Dordrecht, 4th edition, 2012.
- [39] D. C. Leslie. *Developments in the Theory of Turbulence*. Clarendon Press, 1973.
- [40] J. J. Lielpeteris and R. Moreau, editors. *Liquid Metal Magnetohydrodynamics*. Springer Science & Business Media, 2012.
- [41] P. K. Mishra, J. H erault, S. Fauve, and M. K. Verma. Dynamics of reversals and condensates in two-dimensional Kolmogorov flows. *Phys. Rev. E*, 91(5):053005–12, 2015.
- [42] H. K. Moffatt. On the suppression of turbulence by a uniform magnetic field. *J. Fluid Mech.*, 28:571–592, 1967.
- [43] H. K. Moffatt. *Magnetic Fields Generation in Electrically Conducting Fluids*. Cambridge University Press, Cambridge, 1978.
- [44] S. Molokov, R. Moreau, and H. K. Moffatt, editors. *Magnetohydrodynamics: Historical Evolution and Trends*. Springer, 2007.
- [45] R. Monchaux, M. Berhanu, M. Bourgoin, M. Bourgoin, and M. Moulin. Generation of a magnetic field by dynamo action in a turbulent flow of liquid sodium. *Phys. Rev. Lett.*, 98(4):044502, 2007.
- [46] R. Moreau. *Magnetohydrodynamics*. Kluwer Academic Publishers, Dordrecht, 1990.
- [47] U. M uller and L. B uhler. *Magnetofluidynamics in Channels and Containers*. Springer, Berlin, Heidelberg, 2001.
- [48] D. Nath, A. Pandey, A. Kumar, and M. K. Verma. Near isotropic behavior of turbulent thermal convection. *Phys. Rev. Fluids*, 1:064302, 2016.
- [49] M. Negrea and V. N. Cancea. On the stochastic anisotropic sheared magnetic field lines diffusion. *Physics AUC*, 2004.
- [50] S. Oughton, E. R. Priest, and W. H. Matthaeus. The influence of a mean magnetic field on three-dimensional magnetohydrodynamic turbulence. *J. Fluid Mech.*, 280:95–117, 1994.
- [51] Y.-H. Pao. Structure of Turbulent Velocity and Scalar Fields at Large Wavenumbers. *Phys. Fluids*, 8(6):1063, 1965.
- [52] S. B. Pope. *Turbulent Flows*. Cambridge University Press, Cambridge, 2000.

- [53] A. Pothérat. Three-dimensionality in quasi-two-dimensional flows: Recirculations and Barrel effects. *EPL*, 98(6):64003, 2012.
- [54] A. Pothérat and R. Klein. Why, how and when MHD turbulence at low becomes three-dimensional. *J. Fluid Mech.*, 761:168–205, 2014.
- [55] A. Pothérat, J. Sommeria, and R. Moreau. An effective two-dimensional model for MHD flows with transverse magnetic field. *J. Fluid Mech.*, 424:75–100, 2000.
- [56] K. S. Reddy. *Anisotropic Energy Spectrum, Flux and Transfers in Quasi-Static Magnetohydrodynamic Turbulence*. PhD thesis, IIT Kanpur, IIT Kanpur, 2015.
- [57] K. S. Reddy, R. Kumar, and M. K. Verma. Anisotropic energy transfers in quasi-static magnetohydrodynamic turbulence. *Phys. Plasmas*, 21(10):102310, 2014.
- [58] K. S. Reddy and M. K. Verma. Strong anisotropy in quasi-static magnetohydrodynamic turbulence for high interaction parameters. *Phys. Fluids*, 26:025109, 2014.
- [59] P. H. Roberts. *An introduction to magnetohydrodynamics*. Longmans, Green and Co. Ltd., London, 1967.
- [60] P. Sagaut and C. Cambon. *Homogeneous Turbulence Dynamics*. Cambridge University Press, 2008.
- [61] U. Schumann. Numerical simulation of the transition from three- to two-dimensional turbulence under a uniform magnetic field. *J. Fluid Mech.*, 74:31–58, 1976.
- [62] J. V. Shebalin, W. H. Matthaeus, and D. C. Montgomery. Anisotropy in MHD turbulence due to a mean magnetic field. *J. Plasma Phys.*, 29(03):525–547, 1983.
- [63] J. Sommeria. Experimental study of the two-dimensional inverse energy cascade in a square box. *J. Fluid Mech.*, 170:139–168, 1986.
- [64] J. Sommeria and R. Moreau. Why, how, and when, MHD turbulence becomes two-dimensional. *J. Fluid Mech.*, 118:507, 1982.
- [65] B. Sreenivasan and T. Alboussiere. Evolution of a vortex in a magnetic field. *Eur. J. Mech. B. Fluids*, 19:403–421, 2000.
- [66] B. Sreenivasan and T. Alboussiere. Experimental study of a vortex in a magnetic field. *J. Fluid Mech.*, 464:287–309, 2002.
- [67] S. Sundar, M. K. Verma, A. Alexakis, and A. G. Chatterjee. Dynamic anisotropy in MHD turbulence induced by mean magnetic field, *Phys. Plasmas*, 24:022304, 2017.
- [68] B. Teaca, M. K. Verma, B. Knaepen, and D. Carati. Energy transfer in anisotropic magnetohydrodynamic turbulence. *Phys. Rev. E*, 79(4):046312, 2009.
- [69] A. Thess and O. Zikanov. Transition from two-dimensional to three-dimensional magnetohydrodynamic turbulence. *J. Fluid Mech.*, 579:383–412, 2007.
- [70] S. Vantighem, X. Albets-Chico, and B. Knaepen. The velocity profile of laminar MHD flows in circular conducting pipes. *Theor. Comput. Fluid Dyn.*, 23(6):525–533, 2009.
- [71] M. K. Verma. Statistical theory of magnetohydrodynamic turbulence: recent results. *Phys. Rep.*, 401(5):229–380, 2004.
- [72] M. K. Verma. Variable enstrophy flux and energy spectrum in two-dimensional turbulence with Ekman friction. *EPL*, 98:14003, 2012.
- [73] M. K. Verma, A. Ayyer, O. Debligny, S. Kumar, and A. V. Chandra. Local shell-to-shell energy transfer via nonlocal interactions in fluid turbulence. *Pramana-J. Phys.*, 65(2):297–310, 2005.
- [74] M. K. Verma and K. S. Reddy. Modeling quasi-static magnetohydrodynamic turbulence with variable energy flux. *Phys. Fluids*, 27(2):025114–15, 2015.
- [75] M. K. Verma, A. Kumar, and A. Pandey. Phenomenology of buoyancy-driven turbulence: recent results, *New J. Phys.*, 19:025012, 2017.
- [76] A. Vorobev and O. Zikanov. Smagorinsky constant in LES modeling of anisotropic MHD turbulence. *Theor. Comput. Fluid Dyn.*, 22:317–325, 2008.
- [77] A. Vorobev, O. Zikanov, P. A. Davidson, and B. Knaepen. Anisotropy of magnetohydrodynamic turbulence at low magnetic Reynolds number. *Phys. Fluids*, 17(12):125105, 2005.
- [78] O. Zikanov, D. Krasnov, T. Boeck, A. Thess, and M. Rossi. Laminar-Turbulent Transition in

- Magnetohydrodynamic Duct, Pipe, and Channel Flows. *Appl. Mech. Rev.*, 66(3):030802, 2014.
- [79] O. Zikanov and A. Thess. Direct numerical simulation of forced MHD turbulence at low magnetic Reynolds number. *J. Fluid Mech.*, 358:299–333, 1998.